Jean Jacques Christian Georges Cantan

The effect of active grid-generated freestream turbulence on an aeroelastic NACA4412 airfoil

Master's thesis in Energy and Environmental Engineering
Supervisor: R. Jason Hearst
Co-supervisor: Leon Li, Magnus K. Vinnes

June 2021

Master's thesis

NTNU
Norwegian University of
Science and Technology

Jean Jacques Christian Georges Cantan

The effect of active grid-generated freestream turbulence on an aeroelastic NACA4412 airfoil

Master's thesis in Energy and Environmental Engineering
Supervisor: R. Jason Hearst
Co-supervisor: Leon Li, Magnus K. Vinnes
June 2021

Norwegian University of Science and Technology
Faculty of Engineering
Department of Energy and Process Engineering

NTNU
Norwegian University of
Science and Technology

Problem description

Turbulence and structural vibrations are omnipresent in flows of engineering interest, yet they are often ignored in basic assessment of airfoil aerodynamic properties. Numerous previous studies have shown that the lift and drag characteristics of an airfoil are dependent on the incoming flow. In particular, the turbulence intensity and the integral length scale. In these studies, they have often struggled to really explore the parameter space because classic static grids were used to generate the turbulence. This meant that to get high turbulence intensities they had to be very close to the grid where coherent vortex shedding was still present. With previous set-ups, overcoming this limitation was virtually impossible. however, with the new active grid at NTNU, we can generate high intensity turbulence very far downstream of the grid where the flow is homogeneous. This work will place a NACA4412 airfoil in such flows and investigate the dependence of the lift and drag on the incoming flow, as well as investigate the lift variation and vibrations of the airfoil resulting from high intensity turbulence. In particular, both classical turbulent flows and ones with specific frequency peaks will be investigated. This work will result in new knowledge enabling a better overall understanding of how airfoils function in realistic flows.

Summary

Aerodynamic and structural properties of a NACA4412 airfoil have been investigated experimentally in the large closed loop wind tunnel at NTNU. The purpose was to gain insight on how freestream turbulence, which was generated using an active turbulence grid, would impact the properties of the airfoil. The airfoil's manufacture was started before the master thesis, and ended two months after the thesis start. When testing the airfoil in the wind tunnel, the energy contained in the turbulence generated by the newly installed active grid was underestimated. This led to strong vibrations of the airfoil, leading us to adapt the problem description, such that these vibrations would be included in the thesis. The airfoil was Reynolds number independent in our test range for pre-stall angles of attack, with a chord Reynolds number of $Re_c = 2.0 \times 10^5$ limited by the experimental facility. It is shown that the properties of the airfoil were strongly affected by turbulence. The experimental results showed an increase in the critical angle of attack and maximum lift as the turbulence intensity increased, but with negligible effect on the lift slope. The lift variation due to the vibrations was found to increase linearly with increasing turbulence intensity for turbulence length scales less than 1.5 times the chord length. The lift spectra showed a dependence on the active turbulence grid rotating frequency, both when operated randomly as well as with specific frequency peaks. An important error with negative drag coefficients was found and discussed.

Sammendrag

Aerodynamiske og strukturelle egenskaper til en NACA4412-bæreflate har blitt undersøkt eksperimentelt i den store lukkede vindtunnelen ved NTNU. Hensikten var å få innsikt i hvordan freestream-turbulens, som ble generert ved hjelp av et aktivt turbulensgitter, ville påvirke egenskapene til vingen. Produksjonen av vingen ble startet før masteroppgaven, og avsluttet to måneder etter at oppgaven startet. Ved testing av vingen i vindtunnelen ble energien i turbulensen som ble generert av det nylig installerte aktive turbulensgitter undervurdert. Dette førte til sterke vibrasjoner i vingen, noe som førte oss til å tilpasse problembeskrivelsen, slik at disse vibrasjonene ble inkludert i oppgaven. Airfoil var Reynolds nummer uavhengig i vårt testområde, med et akkord Reynolds-antall på $Re_c = 2.0 \times 10^5$ begrenset av eksperimentelle anlegget. Det er vist at propellens egenskaper ble sterkt påvirket av turbulens. De eksperimentelle resultatene viste en økning i den kritiske angrepsvinkelen og maksimal løft etter hvert som turbulensintensiteten økte, men med ubetydelig effekt nei løftehellingen. Heisvariasjonen på grunn av vibrasjonene ble funnet å øke lineært med økende turbulensintensitet for turbulenslengdeskala mindre enn 1,5 ganger akkordlengden. Heisspektrene viste en avhengighet av den aktive turbulensnettets rotasjonsfrekvens, både for klassiske turbulente strømmer og de med spesifikke frekvenstopper. En viktig feil med negative dragkoeffisienter ble funnet og blir diskutert.

Acknowledgements

Contents

List of Figures

List of Tables

Abstract

An aeroelastic NACA4412 airfoil subjected to different incoming freestream turbulence (FST) is investigated experimentally. The FST was generated by an active turbulence grid (ATG) and was divided in two distinct categories: homogeneous and periodic turbulence. The chord Reynolds number $Re_c = 2.0 \times 10^5$ was limited by the facility, and the airfoil was Re_c independent in the pre-stall region. The ATG allowed for the generation of homogeneous turbulence intensities up to $T_i = 17.5\%$. Increasing T_i increased the critical angle of attack and the maximum lift, but had negligible effect on the lift slope. The lift coefficient variation (C'_L) was found to increase linearly with increasing T_i, for turbulence length scales L_{ux} less than 1.5 times chord length. The lift spectra showed a dependence on the ATG's shaft rotating frequency (Ω), with a plateau starting at $f = \Omega$ for frequencies below the resonance frequency of the airfoil; the latter was independent of the flow velocity and T_i. Periodic turbulence resulted in a strong degradation of the airfoil's performance. C'_L was found to be reduced for increased flapping frequency of the shafts (f_f). The vibrations of the airfoil were strongly dependent on f_f and its harmonics, which acted as a second vibration input in addition to the airfoil's natural response.

1   Introduction

Most real world applications of airfoils include variations in their operating conditions, that impact their performance. Real airfoils are also flexible and aeroelastic with, for instance, the wing tip of a B-52 being able to flex by 4.3 meters (Vos and Farokhi, 2015). Stack (1931) investigated, among other things, the effects of turbulence on the lift and drag of rigid airfoils. Increasing turbulence intensity (T_i) or integral length scale (L_{ux}) impacted positively the lift curves for thick airfoils, while thin airfoils did not exhibit a strong dependence on T_i. The turbulence intensity is defined as $T_i = (u'^2)^{1/2}/U$, where u'^2 is the variance of the velocity signal and U is the mean velocity; for simplicity, we will also write the turbulence intensity as u'/U where u' represents the standard deviation. One of the effects also noted by Stack (1931) was the small dependence of the profile drag on T_i at very high Reynolds number. Eight dacades later, this same dependence of airfoils on T_i was observed by Wang et al (2014). Wang investigated the aerodynamics of a NACA0012 airfoil, proposing four regimes of chord Reynolds number (Re_c) with distinct characteristics in terms of its lift coefficient (C_L) and flow structure dependence on angle of attack (α); the ultra-low ($<1.0 \times 10^4$), low (1.0×10^4–3.0×10^5), moderate (3.0×10^5–5.0×10^6), and high ($>5.0 \times 10^6$) regimes. In the ultra-low regime, the separated laminar shear layer does not reattach. The influence of T_i is significant, with C_L and C_L/C_D increased by 52% and 45%, respectively, for T_i=0.6 % to 6.0 %. In the low Re_c regime, the separated laminar shear layer reattaches, forming a separation bubble. For the moderate and high regimes, C_L was strongly dependent on T_i.

Li and Hearst (2021) investigated a wind turbine NREL S826 airfoil subjected to different incoming flows with varying degrees of freestream turbulence (FST). Holding Re_c=4.0 × 10^5 constant, T_i was varied between 0.4% and 5.4%. An increase in maximum lift for an increase in T_i was reported. Periodic pressure fluctuations were observed near the leading edge for T_i between 1% and 2% and the airfoil operating in the linear region. For higher T_i, the fluctuations were suppressed and more energetic boundary layers developed over the suction side, leading to an increase in the produced lift. In their study, no effect was seen on stall angle, also referred to as the critical angle of attack (α_{crit}), for different T_i. Maldonado et al (2015) investigated an experimental low Re_c S809 wind turbine blade with a T_i of 6.14%. holding Re_c at 2.08×10^5. Results showed a significant improvement of the aerodynamic performance of the blade by increasing the lift coefficient and overall lift-to-drag ratio, as well as the lift slope, for all α tested except 0°.

Swalwell et al (2001) studied a NACA0021 airfoil at $Re_c = 3.5 \times 10^5$ over a wide range of angles of attack and T_i varying from 0.6 %, 4% and up to 7%. In contrast to aforementioned studies, Swalwell et al (2001) showed that turbulence delayed stall to higher α_{crit}. This was also shown by Devinant et al (2002), studying a NACA65(4)–421 airfoil used on wind turbines, placed at α up to 90°. High T_i (with intensity up to 16 %) had a major effect on the aerodynamic properties: at higher T_i, the separation point advanced slower towards the leading edge with increasing α. Cao et al (2011) noted that no significant

changes in the lift and drag were present for $T_i = 9.5\%$. Cao investigated the performance of a high-lift wind turbine airfoil S1223 in turbulent flow at Re_c varying from 5.5×10^4 to 1.0×10^5 and α from $-5°$ to $25°$. A T_i of 4.1% appeared to delay the stall, implying a delay in the boundary layer separation on the suction surface.

A controversial topic is the effect of FST on the lift slope $dC_L/d\alpha$, with no clear consensus, and studies in contradiction to one another. Ravi et al (2012) found that for a thin plate subjected to T_i from 1.2% to 12.6%, $dC_L/d\alpha$ decreased with increasing T_i, whereas Li and Hearst (2021), Maldonado et al (2015) and Wang et al (2014) found an increase in $dC_L/d\alpha$ for increasing T_i for a thicker airfoil. Huang and Lee (1999) observed that for T_i of 0.2% to 0.65% on a NACA0012 airfoil, no significant changes were present for $dC_L/d\alpha$, even if a T_i of under 1% appeared to have significant effects on the maximum lift and α_{crit}. Li and Hearst (2021) discussed these contradiction and pointed out that the flow homogeneity, depending on the proximity to the grids, could influence the airfoil properties.

For this study, a NACA4412 airfoil will be studied in a low to moderate Re_c regime. The NACA4412 is a generic reference airfoil used frequently in aircraft. A few examples include the AA-AA2 Mamba aircraft, the Avtech Jabiru LSA/ST, or Aeronca 65-tac Defender. These aircrafts are used mostly for short flights, and transit more often in the atmospheric boundary layer than other aircrafts, where turbulence is often strong due to proximity to the ground (Stewart, 1979). Genç et al (2016) and Koca et al (2018) both investigated NACA4412 airfoils at low Re_c and found that α_{crit} increased for increasing Re_c. The reference properties of the NACA4412 used in this study will be based on the technical report for the U.S. Department of Energy from Ostowari and Naik (1985), with post-stall wind tunnel data for rigid NACA44XX series airfoil sections.

Due to the manufacturing process, the airfoil used in this study is elastic and experiences flow induced vibrations. Most airfoil's flow induced vibration studies tend to focus on classical flutter with 2 degree of freedom (2-DOF) in pitch and heave (Dessi and Mastroddi, 2008; dos Santos and Marques, 2021; Yuan et al, 2021), or a single degree of freedom (SDOF) in pitch (Qiu and Wang, 2020; Wu et al, 2020). Classical flutter is an instability of a wing caused by the change of α due to torsion deformation of the wing. This deformation generates aerodynamic lift forces that are in phase with the flapwise bending motion, potentially leading to structural failure of the wing section. Due to the set-up of the experiment, classical flutter is not observable here reducing the problem to stall induced vibrations, stall flutter and dynamic stall, which are less investigated areas. Dimitriadis and Li (2009) addresses the distinction between dynamic stall, which is purely aerodynamic, and stall flutter, which is a self excited oscillation due to the dynamic stall nonlinear forces, as well as inertial forces and structural properties of the airfoil section. A good way to isolate the structural properties of the airfoil is by conducting a shock-excitation of the airfoil as presented by Fearnow (1951). Fearnow found that the damping characteristics were non-linear due to the viscous damping of air, where the damping coefficient (ξ) depended on the amplitude of the vibrations.

An airfoil with fixed ends in low to moderate Re_c has some similarities with suspended bridges when it comes to its structural properties. Li et al (2021) investigated the effects of L_{ux} on the buffeting response of a long-span suspension bridge, reporting that the Root Mean Square (RMS) of the equivalent buffeting lift forces per unit span increased almost linearly with L_{ux}. They also reported that the effects of L_{ux} were independent of U. In this study, the buffeting of the airfoil is constant through individual cases, and the RMS of the lift time-series is equal to the standard deviation. The effect of L_{ux} was also studied by Vita et al (2020), for a DU96w180 wind turbine airfoil. They reported that for L_{ux} significantly larger than the airfoil's chord length (c), entrainment of the flow in the boundary layer is less efficient. More investigations of the boundary layer forming over the airfoil were done by Goyaniuk et al (2020), who investigated stall flutter of a NACA0012 airfoil. Among other things, they reported that low enough T_i can enable a laminar boundary layer on a significant portion of the airfoil, having an aerodynamic stiffening effect. This was also reported by Poirel and Mendes (2014).

Most set-up used for studying the effects of turbulence on airfoils have used fixed passive grids, resulting in a relatively low number of cases, T_i, and turbulence-based Reynolds numbers. Hearst (2019) shows the range of turbulence intensities and Reynolds numbers achievable by ATGs around the world, and

their importance for model testing. The ATGs allows for the simulation of realistic conditions where T_i is large. Mücke et al (2011) measured the atmospheric T_i between 50 m and 150 m above ground level. On average, T_i was between 5% and 10%, but could reach up to 40%. To generate FST, Maldonado et al (2015) and Ravi et al (2012) both used an ATG, allowing them to investigate greater range of T_i.

The mesh size of the grid, M, determines the integral length scale of the turbulence for passive grids. A large downstream separation is usually needed for the flow to become homogeneous and isotropic, with Cekli and van de Water (2010) reporting a necessary downstream separation of 40 M and Comte-Bellot and Corrsin (1966) reporting that homogeneous isotropic turbulence is achieved at around $x/M = 30$. The decay of isotropic turbulence follows a power-law, depending on the Reynolds number at the grid (Re_λ), determining the level of T_i at a particular x/M (Pope, 2000). For ATGs, the parameters mostly influencing the produced flow are the rotational rate of the shafts, the bulk Reynolds number, and the blockage of the wings (Hearst and Lavoie, 2015). homogeneous, isotropic turbulence is best achieved with a fully random mode of operation of the shafts, with randomized velocity and periods of rotation (Hearst and Lavoie, 2015; Larssen and Devenport, 2011).

It would appear that there is no clear consensus as to what the effects of having airfoils subjected to turbulence are. Even if most of the publications cited here report a general increase in maximum lift and a retardation of the stall angle as T_i increases, some clear differences as to whether the lift slope increases, stays approximately the same or decreases with increasing T_i exist. The setups used by different authors varied, as did the incoming flow conditions and Re_c. A difference in the effects T_i has on the lift slope was noted, and seems to depend on the airfoil profile and thickness. In this study, we are interested in how different incoming FST influences the airfoil performance and characteristics discussed thus far. The structural properties and vibrations of the airfoil will also be looked at, with a focus on their relation to FST.

Section 2 will describe the experimental set-up. Section 3 will describe the incoming flow characteristics. In section 4, the airfoil structural properties and response will be presented. Section 5 will describe the mean forces and moment for: the Reynolds number scans, the homogeneous and the periodic incoming turbulence. In section 6, the time-series and vibrations will be analysed in the time and frequency domain. Section 7 will describe further work and possible improvements of the experiments, and section 8 will present the conclusions drawn from this work.
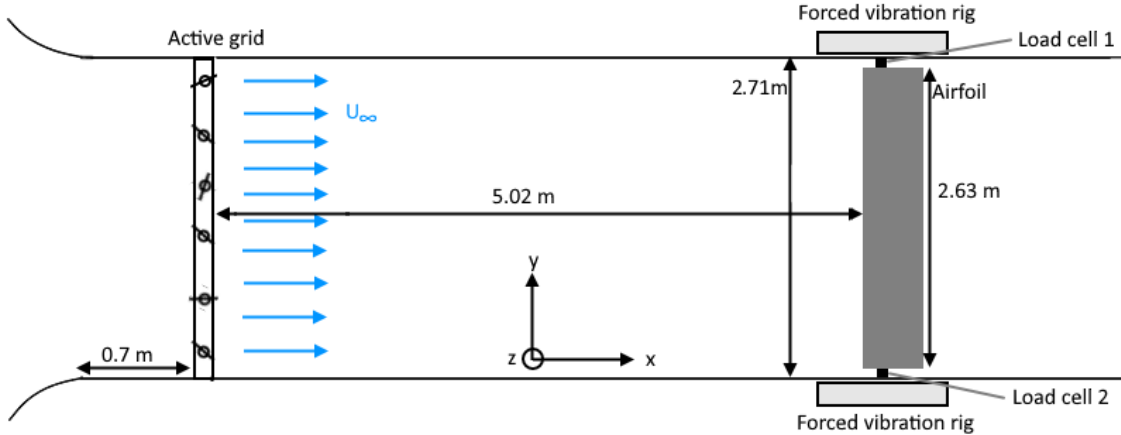
Figure 1: Experimental set-up from a top view. The schematic is not to scale.

2 Experimental apparatus and set-up

The closed-loop wind tunnel at the Norwegian University of science and Technology was used to conduct this experiment. The test-section is 1.80 m× 2.71 m, with a length of around 11 m. The flow is induced by a 220kW fan located downstream of the test section. The flow velocity was varied between 5 m/s and 20 m/s, corresponding to $Re_c = 1.0 \times 10^5$ and $Re_c = 4.1 \times 10^5$, respectively. A schematic of the setup is presented in Figure 1.

The NACA4412 airfoil was manufactured with a single beam as the spar, 3D printed ribs and an iron-on type polyester fabric covering for the skin. Thin 3D printed structures placed between the ribs were used for the leading and trailing edges to help the fabric take the correct form at these locations. The model has a span b of 2630 mm, and a chord c of 310mm, giving an aspect ratio AR of 8.48 and a surface area $S = 0.82$m^2. No end plates were used as high aspect ratio (AR>6.7) tends to minimize vortex shedding as discussed by Szepessy and Bearman (1992). In addition, the edges of the airfoil section are located 40 mm from the wall, or $0.13c$, which limits the formation of tip vortices and means the tunnel walls effectively act as end plates (Bartl et al, 2019). The spar is a 20 mm×40 mm×2710 mm extruded aluminium beam placed at $c/4$ with a Young's modulus $E = 70 \times 10^3$ N/mm and the area moment of inertia of the cross section is $I = 14.1 \times 10^6$ mm^4. These properties give a theoretical maximum deflection $\delta_{max} \approx 5$ mm for an evenly distributed load of 100 Newtons as a rough estimate of the maximum net lift load. This is the only structural member in the assembly, and thus its properties represent the main structural properties of the airfoil. In total, the model weighed 3980 grams, including a pressure scanner of 220 grams placed in the centre of the model used for other experiments. Ground effect correction was not applied as the airfoil is placed 900 mm or $z/c = 2.9$ above the floor of the test section (Qu et al, 2014). The blockage ratio at $\alpha = 20°$ is 3.9%, which is sufficiently small such that blockage corrections are not required (West and Apelt, 1982; Zhou et al, 2019). The leading edge of the airfoil is located at $x = 5020$ mm $= 50.2M = 16.2c$ downstream of the ATG where the flow is homogeneous, see section 3 (Cekli and van de Water, 2010; Comte-Bellot and Corrsin, 1966). Pictures of the airfoil construction are included in Appendix A.

Both ends of the model were mounted to a forced vibration rig (Siedziako et al, 2017), consisting of one 3 degrees of freedom actuators on each side of the wind tunnel. These actuators are comprised of linear motion slides for vertical and horizontal displacement driven by ball screws. Zero backslash shaft couplings connect the ball screws to servomotors and a servo motor with a planetary gear with a 1:50

gear ratio drives the torsional motion. For this experiment, only the torsional motion was used in order to control the angle of attack of the airfoil varying it from $-8°$ to $20°$. The torsional axes can travel $\pm90°$ and are controlled using a customized multi-axis modular control system (MC4U from ASC Motion Control) with a SPiiPlus motion controller. For more information about the forced vibration rig, see Siedziako et al (2017).

Two ATI Industrial Automation Gamma load cells fixed between the actuator and the model ends were used to measure all six forces and moment about the x, y and z axes. The load cells are bolted to the stage and the model was clamped to the load cell. The combination of the six measured forces and moments is acquired simultaneously for both load cells with a sampling rate of 200 Hz and an accuracy of $1/40$ N. The net forces L, D and M acting on the airfoil are then obtained by combining the signal of both load cells, and removing the mass of the airfoil scanned for each α with no flow. The mass scans were performed before the other test cases and the airfoil was then removed from the load cells after marking its position. When remounting the airfoil, the inaccuracy was of order $0.5°$. The airfoil was not removed between cases with similar flow characteristics. The non-dimensionalized lift, force and moment coefficients are then

$$C_L = \frac{L}{\frac{1}{2}\rho_\infty U_\infty^2 S} \ ,$$

$$C_D = \frac{D}{\frac{1}{2}\rho_\infty U_\infty^2 S} \ ,$$

$$C_M = \frac{M}{\frac{1}{2}\rho_\infty U_\infty^2 S c} \ ,$$

where ρ_∞ is the freestream fluid density estimated with a pressure transducer integrated to the forced vibration rig and a thermocouple in the test section, and U_∞ is the freestream velocity obtained with a Pitot-static tube. Both instruments are placed close to the model and can be seen in Figure 2. Similar methods for force measurements were used by Cigada et al (2001) and Han et al (2014).

The active turbulence grid can be seen in Figure 2. It is located in a slot 700 mm downstream of the test section inlet and has the same cross-section as the test section. Its inner walls are $\pm$ 1mm flush to the test section's wall and the grid sides are sealed with tape such that no flow leaks through the connection. The ATG is made of orthogonal rods with vanes attached to them. Each vertical rod includes eighteen square vanes with a diagonal of 95 mm, spaced evenly 100 mm apart. The horizontal rods include twenty-seven similar vanes, also spaced 100 mm apart, giving a mesh size $M = 100$ mm. An interior support superstructure is present due to the large size of the grid. One horizontal bar is located at mid-height giving a blockage of 9.7 mm of the flow, which is similar to the blockage from the rods. Three 12.7 mm thick vertical bars are located at the center of the structure as well as 700 mm on either side of center. The vertical bars are notched such that vertical vanes placed right after them rotate freely. The upstream edges of the superstructure are rounded, streamlined profiles and the downstream edge of the horizontal bar is tapered to reduce generation of turbulence by the bar itself. In total, the active turbulence grid consists of 90 shafts (rod with vanes), each controlled by a dedicated integrated stepper motor (Applied Motion Products Model No. STM23S-3RE), each including an integrated drive and encoder. The stepper motors are supplied by a total of fifteen 48VDC power supplies, allowing for an adjustable speed range up to approximately 18 Hz. With the active turbulence grid turned on, the flow was limited to ~ 10 m/s corresponding to a chord Reynolds number $Re_c \approx 2.0 \times 10^5$ with $Re_c = \frac{\rho_\infty U_\infty c}{\mu}$, where μ is the fluid dynamic viscosity.

To achieve homogeneous, isotropic turbulence, the shafts were operated in four random modes, with randomized acceleration, periods of rotation, and a rotational velocity $\Omega \pm \omega$, where ω is a random frequency ranging $\frac{1}{2}\Omega$, as proposed by Hearst and Lavoie (2015) and Larssen and Devenport (2011). This was done to cover a broader range of turbulence and allow for relatively stable turbulence properties

Figure 2: Airfoil mounted to the load cells and forced vibration rig in the test section. Also visible: the active turbulence grid in the background, the Pitot-static tube under the airfoil on the left side, and the thermocouple on the right wall, just under the airfoil section.

during each case. In addition, the shafts were also operated in four periodic modes, with the shafts flapping at $\pm\theta$ with a flapping frequency f_f. The shafts were separated in four regions along the horizontal and vertical midlines, with the diagonally opposed regions flapping at the same angle, and the adjacent regions flapping at opposed shaft angles. The different operating modes of the grid are presented more explicitly in section 3.

Turbulence characterization at the airfoil's leading edge position, with the airfoil removed, were performed using a Dantec 55P21 X-wire probe controlled via a Dantec StreamLine Pro Constant Temperature Anemometer. The wires have a diameter of 5 μm and a sensing length of 1.25 mm. It was mounted to an electrical rotary stage, which was in turn attached to a set of beams that allowed movement in both the $y-$ and $z-$directions. The rotary stage allowed for in-situ X-wire calibration, which was performed at the beginning and end of each day. A Pitot-static tube and a temperature probe were also mounted to the static frame of the rotary stage close to the X-wire. The tip of the X-wire probe coincided with the location of the leading edge of the airfoil at centre span. The characterizations were performed at the same wind tunnel speed setting for each case, and calibrations were performed for 1.1 m/s $\leq U_\infty \leq$ 18 m/s, and for X-wire probe angles up to $\pm45°$. The data acquisition was conducted through a computer via a NI DAQ system, and the rotary stage was also controlled through the computer during calibrations. The X-wires were operated at an overheat ratio of 1.8, and data were sampled at 75 kHz, with the internal anemometer low-pass filter set at 30 kHz. The sampling time varied from 300 s to 600 s depending on the ATG cases, the spectra of the raw X-wire signals were checked after each acquisition to ensure convergence in the low-frequency content. In the post-processing for the X-wire data, the Kolmogorov frequency f_η was estimated for the computed velocity time-series, and a 7$^{\text{th}}$-order digital low-pass Butterworth filter was applied to the time-series at 1.1f_η. Homogeneity scans were performed with a Pitot-static tube for a reference case without the ATG, a static ATG case and the more extreme ATG cases. The scans were made at the same streamwise-location as the leading edge of the airfoil, $z =$900 mm above the floor, and at 13 measurements points equally spaced by $y =$ 200 mm. Only one homogeneity scan was performed for the static grid case and the no grid case, which had varying flow velocities to determine when the airfoil section became Reynolds number independent. These cases

6

Case	$\Omega \pm \omega$ [°±Hz]	U_p [m/s]	T_i [%]	u'/w'	L_{ux}/c	Re_λ
REF	—	10.19	1.11	1.12	0.06	69
H02	—	10.34	1.99	1.23	0.26	74
H11	7±3.5	9.82	10.9	1.39	0.95	489
H12	5±2.5	9.93	11.6	1.35	0.82	513
H16	1±0.5	9.94	16.4	1.39	1.22	819
H18	0.5±0.25	9.89	17.5	1.54	2.00	968

Table 1: Properties of the incoming flow for homogeneous active turbulence grid cases.

Case	θ [°]	f_f [Hz]	U_p [m/s]	T_i [%]	u'/w'	L_{ux}/c	Re_λ
REF	—	—	10.20	1.11	1.12	0.06	69
F15a	15	0.4	9.34	7.68	2.41	0.95	748
F15b	15	4	9.89	15.0	3.25	0.52	1458
F45a	45	0.4	8.34	55.8	2.42	1.76	1931
F45b	45	4	9.65	22.8	1.60	0.36	724

Table 2: Properties of the incoming flow for periodic active turbulence grid cases.

were still regarded as representative, since homogeneity in grid turbulence is typically Reynolds number independent (Larssen and Devenport, 2011), and these cases had both a $T_i < 2\%$.

3 Incoming flow characteristics

The characteristics, velocity profiles and spectra of the different incoming FST cases are presented in this section. The results of the measurements for the flapping cases are also brought into question.

3.1 Homogeneity

The incoming mean velocities normalized by the centreline velocity, U/U_c in the z and y direction measured with hot-wire anemometry for the cases from Table 1 and Table 2 are given in Figure 3 and Figure 4, respectively. The Taylor microscale Reynolds number, i.e., the Reynolds number typically used to characterize the turbulence, is also provided in Table 1 and Table 2. It is calculated from

$$Re_\lambda = \sqrt{u'^2}\frac{\lambda}{\nu} \ ,$$

where $\lambda^2 = \frac{u'^2}{(du'/dx)^2}$. These equations assume isotropy. While the present measurement method allows for less strict assumptions, we use the isotropic definition because they are the most prevalent in the literature and thus the quantities most readily compared between studies.

For the random cases, as the rotational speed of the shafts $\Omega \pm \omega$ was decreased, T_i increased (Table 1). The elevated turbulence resulted in improved homogeneity in both y and z with smaller U/U_c variations. The profiles of the flapping cases are less homogeneous than for the random ones, with higher U/U_c. This supports Hearst and Lavoie (2015), who also found that random ATG cases were the most homogeneous. In Figure 3, a depression in the profile is observed around the centre points for the static cases. This effect is believed to be caused by the horizontal support bar of the ATG superstructure located at the same position as this depression (the bar can be seen in Figure 2). All the random ATG cases are able to suppress this depression, with no $U > U_c$. In the y direction, an inverted velocity gradient, with higher velocity towards the walls, is present for the REF case and the flapping cases, up to $U = 1.2U_c$ for case F45b. It is less clear why this gradient does not decay near the walls, but the blockage from the support and the periodicity of FST combined with the vertical bars superstructure are suspected to be the causal factor.
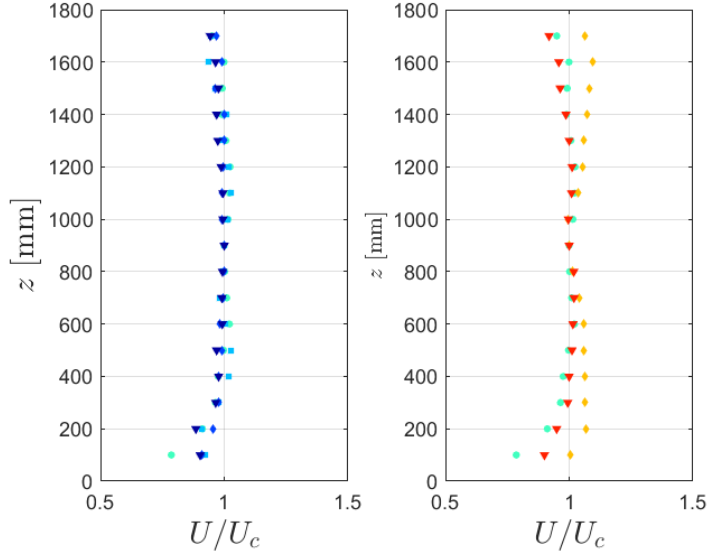
7

Figure 3: Flow homogeneity profile in z for cases: H02($\square$), H11($\diamond$) and H18($\triangledown$) on the left, and cases: F15b($\diamond$) and F45b($\triangledown$) on the right, with REF($\circ$) on both.

3.2   Random cases

The incoming flow properties for the different homogeneous FST cases generated by the random ATG protocols are presented in Table 1. U_p is the mean velocity measured by the Pitot-static tube from Figure 2, and is the only velocity used for later calculations. As $\Omega \pm \omega$ was decreased and U_p kept relatively constant by adjusting the wind tunnel fan rpm, T_i, the fluctuating isotropy ratio u'/w' and the integral length scale L_{ux}/c all increased. FST ranges from $T_i = 10.9\%$ for the fastest shaft velocity up to $T_i = 17.5\%$ for the lowest. For these cases, less than 0.01 % of the data was outside the calibration range.

3.3   Flapping cases

Table 2 shows the incoming flow properties generated by the flapping ATG cases. Flapping the shafts at different angles θ gave different characteristics. Increasing f_f for $\theta = 15°$ increased T_i and u'/w', but reduced L_{ux}/c. For $\theta = 45°$, increasing f_f reduced T_i, u'/w' and L_{ux}/c with up to 4 % of the data outside the calibration range. It should be noted here that T_i of 55.8 % as reported by the hot-wire is not a trustworthy result. Hot-wires are usually limited to T_i up to $20 - 25\%$ (Bruun, 1995). Basing the properties on mean velocity is also not very representative of the flow, as the shafts are flapping periodically. Further investigation of the hot-wire data showed a periodic pattern of velocities down to 2 m/s alternating with gusts up to 18 m/s, as presented in Figure 5c and Figure 5d.

The one-dimensional velocity spectra, ϕ_u for all cases except REF is shown in Figure 6. The units are deliberately not normalised as future spectra are kept dimensional. It is meaningful to see the actual frequencies in dimensional space to compare vibrations with excited frequencies in the turbulence measurements and at the grid. Thus, it isn't clear what non-dimensionalisation should be used for the frequency axis or corresponding spectrum axis. This also illustrates the increase in energy across the cases, as T_i increases. ϕ_u represents the density of contributions to the kinetic energy per frequency, and $f^{-5/3}$ is the Kolmogorov-Obukhov 5/3 law for the inertial range of a homogeneous, isotropic turbulent flow. For the random cases, as T_i increases, ϕ_u approaches $f^{-5/3}$ more closely, indicating a fully developed turbulent free stream at the airfoil location. The flapping cases on the other hand are not as well developed, with case F15b showing two distinct peaks in ϕ_u at $f = 6.87$Hz and $f = 13.74$Hz, and F15a

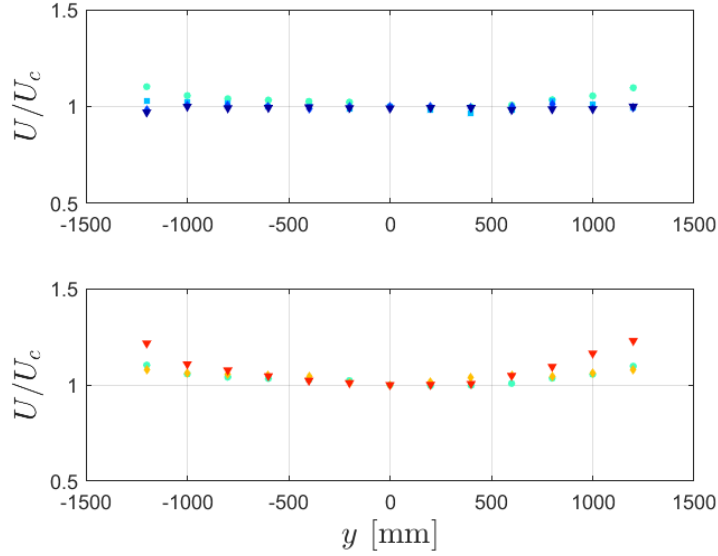Figure 4: Flow homogeneity profile in y for cases: H02($\square$), H11($\diamond$) and H18($\triangledown$) on the left, and cases: F15b($\diamond$) and F45b($\triangledown$) on the right, with REF($\circ$) on both.

a less distinct peak at $f = 3.5$. At higher f, the flapping cases follow the $f^{-5/3}$ range more closely. For F45a and F45b, a collapse of the periodicity is suspected as ϕ_u is brought closer to a $f^{-5/3}$ slope even for lower frequencies. This also observed in Figure 5d, with a less periodic pattern than for Figure 5c. In addition, the frequencies where the periodicity is contained were not resolved because the spectra never round off at low frequencies like it does for the other cases. This means that the sampling time was not long enough to converge that part of the spectrum, but as the periodicity is at very low frequencies, that would give a sampling time greatly higher than 10 minutes that were used here.

Due to the strong periodicity of the F15 cases and suspiciously high T_i for the F45 cases, the turbulent properties assessed for the flapping ATG cases are considered suspect. They are, however, helpful in understanding the high magnitude of the FST for these cases. For these cases, the flow is regarded as periodic, with increased gust intensities at higher θ, and increased gust frequency with higher f_f. The random ATG cases are homogeneous. We have confidence in the flow we produced and measured for the random cases, however, for the flapping cases we find the results more suspect. The flows are highly periodic and the parameters exceed that which hot-wires can reliably measure. Therefore, we are less trustful of the results from those cases.
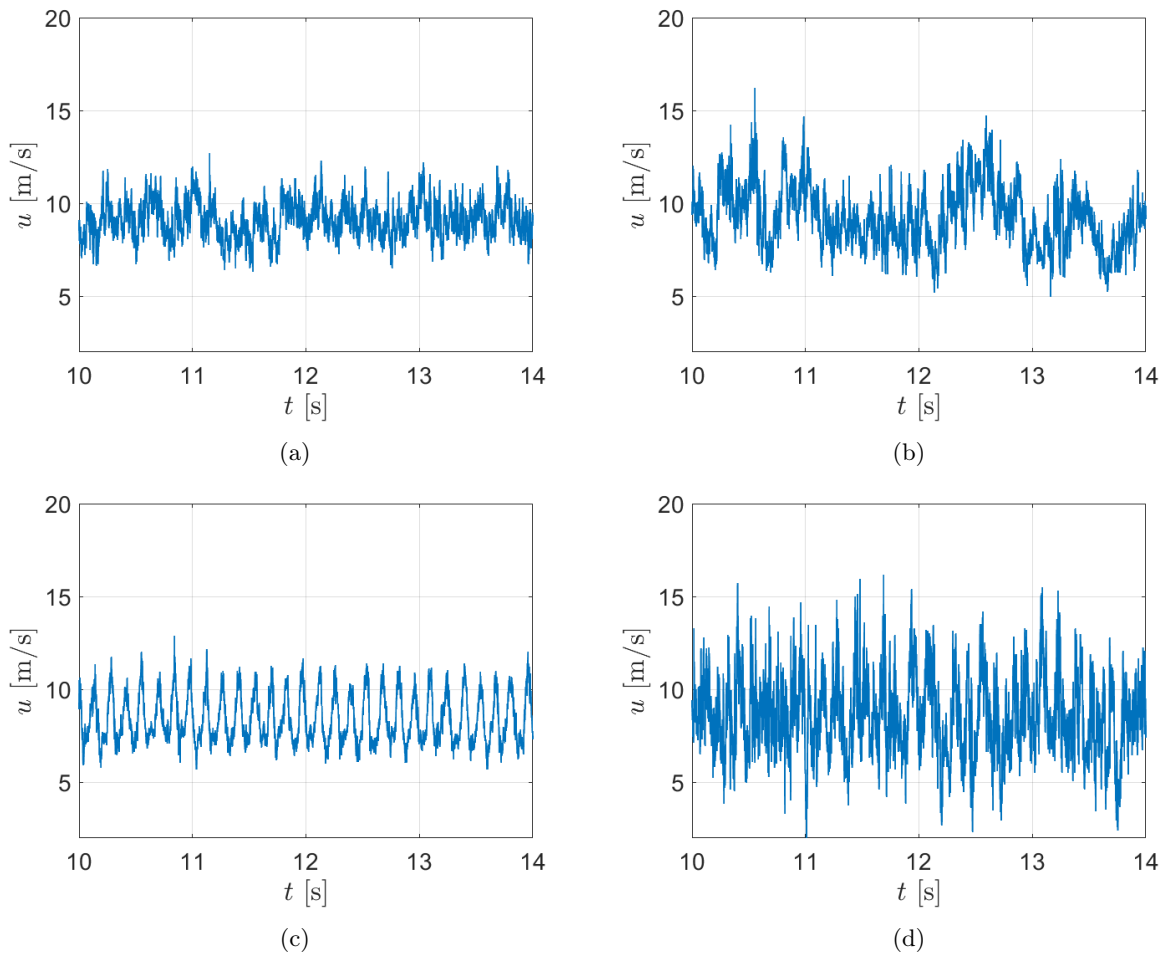
Figure 5: Time-series of hot-wire measured velocity at the centre point for (a) H11, (b) H18, (c) F15b and (d) F45b. The axes are left dimensional in order to visualise the absolute differences in the signals.
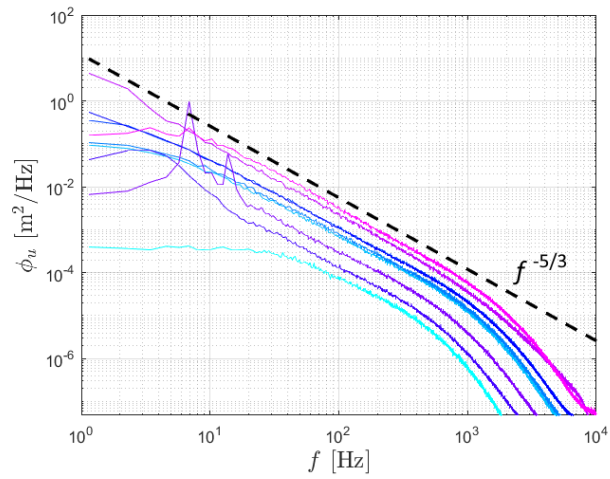
Figure 6: Dimensional free-stream velocity spectra for all ATG cases with increasing color intensity corresponding to increasing T_i: H02 to H18 (Light blue to dark blue) and F15a to F45b (dark magenta to light magenta). The spectra are deliberately left dimensional in order to see the relative change in variance as well as to see the dimensional frequencies of the peaks.
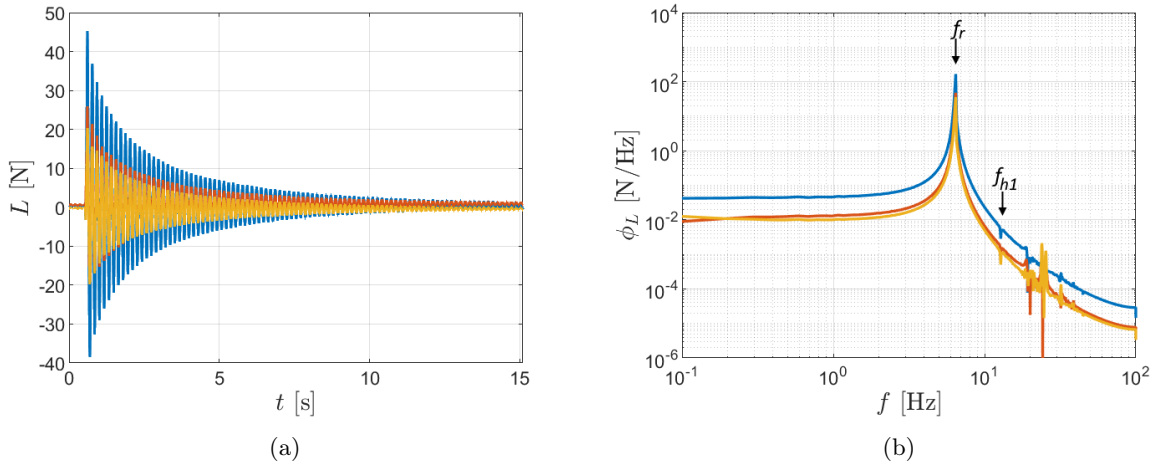
11

Figure 7: Time-series of shock-excitation test (a) and corresponding power spectral density (b) with F_{z1}(—) the force measured with load cell 1, F_{z2}(—) load cell 2 and $L = Fz1 + Fz2$(—).

4   Model properties and response

Both ends of the model are clamped and allow no motion in the torsional direction at the load cells. The elastic centre (i.e., the beam) is placed at the aerodynamic centre $c/4$ (Ostowari and Naik, 1985) giving a theoretical infinite torsional divergence speed (Hodges and Pierce, 2011). This study will therefore mainly focus on force fluctuations occurring in the lift direction, due to unsteady deflection of the airfoil by the turbulent flow.

A modal impact test, i.e. a shock-excitation test with zero flow velocity, allows for more insight to the structural dynamics. Figure 7a presents the recorded force in the lift direction, here L for simplicity, of a shock-excited, vibration test of the airfoil. The airfoil vibrated at a resonance frequency $f_r = 6.5$ Hz. The first couple of cycles, as well as cycles towards the very lowest amplitudes, before and after the excitation, showed an indication of a higher frequency being superimposed upon the resonance frequency. The time-series of the forces were digitally filtered with a 7th-order low-pass Butterworth filter to remove frequency associated with the noise floor. The cutoff frequency was set to $f_c = 40$ Hz, a value within the required Nyquist frequency for the cutoff (Shannon, 1949). Figure 7a shows that the signals from the two load cells are in good agreement with similar amplitude and phase. The net force acting in the lift direction is then obtained by combining F_{z1} and F_{z2}, giving an underdamped mass-spring-damper system. Similar to Fearnow (1951), viscous damping in air gave a non-linear damping coefficient, ranging here from $\xi = 7.82 \times 10^{-3}$ to $\xi = 2.22 \times 10^{-3}$ for the intervals where $L = 30 \pm 10$ N and $L = 5 \pm 2$ N, respectively. Later on, specific ξ corresponding to the amplitude of the vibration will be used when needed. It is interesting here to compare f_r with the resonance frequency from the properties of the beam where $f_r = \frac{13.86}{2\pi} \sqrt{\frac{EIg}{ML^3+0.383wL^4}} = 12$ Hz (Young and Budynas, 2002). In reality, E is reduced by the other structural components of the airfoil with much lower tensile stiffness, while I remains relatively unchanged; the contribution from the thin fabric located far from the centre is much lower than the beam's component (Brahma and Mukherjee, 2010). If the other constants are unchanged, this would give $E = 20.3 \times 10^3$ N/mm to achieve $f_r = 6.5$ Hz.

Figure 7b shows the corresponding Power Spectral Density (PSD) ϕ_L for the same shock-excitation test. The area under the ϕ_L curves represents the Root Mean Square (RMS) value, here equal to the standard deviation $L' = \sqrt{\frac{1}{N-1} \sum_{i=1}^{N} |L_i - \overline{L}|^2}$, for the time-series of L with N observations, where $\overline{L}$ is the mean of L. L' relates to the power of the sinusoid from the time-series in Figure 7a and is expressed in Newtons. To obtain ϕ_L, an FFT was computed with 2^{11} bins, from the filtered signals from each load cells as well as their combined signal.

Both signals from the load cells are in good agreement, and the combined signal is slightly higher. The highest peak where $\phi_L = 10^2$ is present at the resonance frequency, $f_r = 6.5$ Hz, in agreement with Figure 7a. Small drops in ϕ_L are present for multiples of f_r, and are the modes of vibrations of the airfoil at higher harmonics $f_{h1} = 13$ Hz, $f_{h2} = 19.5$ Hz up to $f_{h6} = 39$ Hz before the cutoff frequency of the filter $f_c = 40$ Hz. Different from the harmonics, one peak is present for both load cells with $\phi_L = 10^{-2}$ at $f_v = 24$ Hz, but is "missed" by the combined signal. This peak is due to higher frequency superimposed upon the resonance frequency at low amplitudes. These frequencies are above the resonance frequency, resulting in a 180° phase shift between the base and the mass (Divincenzo, 2020), and are therefore cancelled by each other when combining their signals. The 15 Hz $< f <$ 22 Hz region is less clear with an agitated ϕ_L, but no specific peak are standing out. The PSD of the other force components for the shock-excitation test were investigated, all having the same f_r, indicating that the airfoil is well restrained in torsional motions.

Standard deviation values from L gave trustworthy results and are used to compute the standard deviation of the time-series reported to the lift coefficient, C'_L in subsection 6.1. As F_{z1} and F_{z2} are in good accordance, and frequencies above f_r tends to cancel each other, future ϕ_L are computed from only one load cell.

5 Mean forces and pitching moment

In this section, the time-averaged force measurements are presented as the time-averaged lift, drag and moment coefficients for the different incoming flow conditions at different α.

5.1 Reynolds number scans

As presented in section 1, the influence of Re_c can be significant on the lift characteristics. Tests were carried out from $Re_c = 1.0 \times 10^5$ to $Re_c = 4.0 \times 10^5$ with turbulence intensities $T_i = 1.11\%$ and $T_i = 1.99\%$ to survey Reynolds number dependant characteristics of the lift, drag and momentThe higher turbulence intensities were not used because active grid turbulence is dependent on the freestream velocity Hearst and Lavoie (2015), so performing a Re scan would result in each Re having a different TI, and thus represent a mixed result. Figure 8a shows the lift coefficient C_L for $T_i = 1.11\%$ at different α. It can be seen that for increasing Reynolds number, the linear section of the lift curve seems to be displaced towards lower C_L with a lift slope relatively constant of around $dC_L/d\alpha = 5.50$/rad. This lift slope is slightly higher than 5.16 reported by Ostowari and Naik (1985), but lower than 2π for thin airfoils. For $Re_c = 2.0 \times 10^5$ to $Re_c = 4.1 \times 10^5$, the maximum lift coefficient $C_{L,max} = 1.31$ is reached at $\alpha_{crit} = 12°$. For $Re_c = 1.0 \times 10^5$, $C_{L,max} = 1.29$ at $\alpha_{crit} = 11°$. Stall is more distinct for Reynolds numbers of the low regime proposed by Wang et al (2014), with a stronger collapse of C_L for $Re_c \leq 2.0 \times 10^5$.

This strong collapse is also well observable in Figure 8c, where C_D stops increasing after reaching α_{crit}. Increasing Re_c tends to give higher α_{crit}, which is in agreement with different studies of other NACA4412 airfoils (Genç et al, 2016; Koca et al, 2018). The decreasing trend of C_D at high α appears to depend strongly on Re_c, with the drag curves decreasing from an α higher than α_{crit}. This effect is suspected to be caused by the separation of the boundary layer, reducing the induced drag due to lift. An interesting point to notice is that even if $\alpha_{crit} = 12°$ for all $Re_c \geq 2.0 \times 10^5$ cases, C_D starts decreasing at higher α for higher Re_c, indicating that the boundary layer has a tendency to stay more attached to the airfoil's surface at higher Reynolds numbers. For even higher α, it is suspected that the C_D curves should regroup together and increase. One should also note here that for α close to 0, the C_D curve is slightly negative. This will be discussed in details in section 7. The corresponding moment coefficients C_M are presented in Figure 8e. It can be seen that higher Re_c tends to give higher C_M, and C_M for $Re_c \geq 3.1 \times 10^5$ agree relatively well.

Reference measurements from Ostowari and Naik (1985) at $Re_c = 2.5 \times 10^5$ are also plotted for their corresponding coefficient and α. The C_L coefficients are well in agreement, with the curve slightly shifted to the right by $\alpha \approx 2°$. This would mean that the difference between our $\alpha = 0$ is slightly different. As the main interest in this thesis is the evolution in behavior at different conditions, this shift is extraneous. The C_D curves are not matching as a different method is used to measure drag. Here, we used force measurements and the total drag is measured, but Ostowari and Naik (1985) used wake rake surveys (i.e. pressure measurements) for this α range, which does not include friction drag.

The C_L, C_D and C_M curves indicate a behavior of the airfoil effectively Reynolds number independent for $Re_c \geq 3.1 \times 10^5$. For the reference test $Re_c = 2.0 \times 10^5$ corresponding to the highest range of Re_c achievable with the ATG, the airfoil is Reynolds number independent for pre-stall α.

Figures 8b, 8d and 8f show C_L, C_D and C_M respectively for $T_i = 1.99\%$. The coefficients appear to have the same general behavior for different Re_c compared to what was observed for $T_i = 1.11\%$, supporting the Reynolds number independence explanation given about the behavior of the airfoil. With a more distinct displacement of the lift curves towards lower C_L, the zero-lift angle of attack is $\alpha_0 = -5°$ for $Re_c \leq 3.1 \times 10^5$ and $\alpha_0 = -4°$ for $Re_c \geq 3.5 \times 10^5$. Other changes are a $C_{L,max} = 1.33$ for $Re_c = 2.0 \times 10^5$ slightly higher than for $T_i = 1.11\%$, and a change in the critical angle of attack; $\alpha_{crit} = 12°$ for $Re_c \leq 3.1 \times 10^5$ and $\alpha_{crit} = 13°$ for $Re_c \geq 3.5 \times 10^5$. The stall of the airfoil also appears to be less pronounced for low Re_c, with C_L and C_D collapsing less at high α. The moment coefficients from Figure 8f are slightly lower than for $T_i = 1.11\%$, and the absence of a drop in the C_M curve at $Re_c = 1.0 \times 10^5$ for $\alpha = -6°$ and $\alpha = -8°$ suggests that flow separation under elevated

Case	α_0	$dC_L/d\alpha$	$C_{L,max}$	α_{crit}
REF	-5°	5.50/rad	1.32	12°
H02	-5°	5.52/rad	1.33	12°
H11	-5°	5.72/rad	1.47	15°
H12	-5°	5.56/rad	1.47	15°
H16	-5°	5.29/rad	1.43	18°
H18	-5°	5.48/rad	1.48	18°

Table 3: The effect of incoming homogeneous, isotropic freestream turbulence on; the zero lift angle of attack, the lift slope, the maximum lift coefficient and the critical angle of attack.

freestream turbulence (FST) is delayed. This behavior is consistent with the observations of previous studies (Swalwell et al, 2001; Devinant et al, 2002; Li and Hearst, 2021).

5.2   Effect of homogeneous turbulence

Figure 9a presents C_L for homogeneous, isotropic FST varying from REF where $T_i = 1.11\%$ to the H18 case where $T_i = 17.5\%$ for all α. Interestingly, the C_L curves are not displaced towards lower C_L, but rather appear to have a slight change in their lift slope $dC_L/d\alpha$ with an increasing trend for increasing $T_i \leq 12\%$ as listed in Table 3. This is in accordance with Li and Hearst (2021), Maldonado et al (2015) and Sarlak et al (2014) recording a general increase in $dC_L/d\alpha$ with FST ranging from $T_i = 0.1\%$ up to $T_i = 6.14\%$. On the contrary, cases H16 and H18 give a different trend as $dC_L/d\alpha$ is lower than for REF. It is not clear why the trend suddenly changes for the last two cases. This could be related to high T_i, and would be consistent with Devinant et al (2002) and Ravi et al (2012), who reported a decrease in $dC_L/d\alpha$ with FST up to $T_i = 15.4\%$ and 12.6%, respectively. Another possible cause for this change in trend could be related to the integral length scale, of $L_{ux}/c = 1.22$ for H16 and of $L_{ux}/c = 2.00$ for H18, while all the other test cases presented $L_{ux}/c < 1$. Nonetheless, the changes in $dC_L/d\alpha$ are too low to give a clear general trend.

The C_D curves of Figure 9b show increasing C_D for increasing T_i. The behavior of the C_D curves follow the same behavior as C_L. The lift is decreasing less for high T_i than it is for REF at post-stall α, almost reaching a plateau. This causes the lift induced drag to still have an important component and therefore, the decrease of C_D in the post stall region is less important for high T_i, with almost no reduction in C_D for $T_i \geq 16.4\%$. For high α before stall, the C_L and C_D curves are higher for $10.9\% \leq T_i \leq 11.6\%$ than for the other test cases. This is due to the change in $dC_D/d\alpha$, which decreases for the two highest FST cases, thus shifting $C_{L,max}$ towards higher α.

From Figure 9c, the C_M for $T_i = 16.11\%$ in the low to moderate α region are higher than for the H16 and H18 cases. This can be related to the integral length scale L_{ux} of the FST higher than c. Indeed the eddies can "miss" the airfoil, and less energy would be transferred to the boundary layer than for $L_{ux} < c$ (Vita et al, 2020). Around α_{crit} for $T_i = 1.11\%$, higher T_i tends to minimize the drop in C_M. In this study, it was not possible to measure the separation bubble location, or whether a separation bubble was present at all. However, both Istvan et al (2018) and Li and Hearst (2021) studied this phenomenon and noted a the delay of the separation bubble as FST increased, we suspect that the same phenomenon is taking place here, hence lowering the loss of moment due to a separation of the flow. For $T_i = 16.4\%$ and $T_i = 17.5\%$, no sudden drop of C_M is present in that region even if the curves have a decreasing trend. This suggests that the separation bubbles are suppressed by very high T_i.

5.3   Effect of periodic incoming turbulence

As stated in subsection 3.3, for the flapping ATG cases, the flow is regarded as periodic, with increased gust intensities at higher θ, and increased gust frequency with higher f_f. C_L of the different periodic cases are shown in Figure 10a. In contrast to the homogeneous turbulence, the periodicity has a general negative impact on the performance of the airfoil. F15a and F15b with $f_f = 0.4$ Hz and $f_f = 4$ Hz are the

only cases with C_L matching partially with the linear region of REF. As α increases, $dC_L/d\alpha$ decreases, but no clear stall was observed. Increasing f_f had a positive impact on the lift curve, as F15b is the only case with lift coefficient clearly above REF. With a low f_f, the airfoil is allowed to buffet longer before a new gust passes over the section. This up and down buffeting motion results in an apparent flow coming from a very different α and causing a flow detachment on one side of the airfoil, reducing its performance. This effect is amplified when increasing the flap angle to $\theta = 45°$, with the slope of C_L not resembling a normal lift curve at all for F45a (Ostowari and Naik, 1985). This indicates that the airfoil is buffeting for all α, and the airfoil is constantly having one of its surface boundary layers detached. At $\theta = 45°$, the increase of f_f resulted in an improvement of C_L. It is suspected that the periodicity of the turbulence partly collapses, as discussed earlier. This is suspected to be caused by a flapping angle and frequency too elevated causing partial stall around the vanes of the ATG. A more random like behavior of the flow still presenting some kind of periodicity explains the improvement of C_L. This will be further investigated in subsection 6.2.

The C_D and C_M curves are also in agreement with the presented effects of periodic FST for the lift. As the buffeting is increased, C_D becomes higher at low α, before the flow detaches on alternating surfaces resulting in reduced drag from the lift component at higher α. The main component on the drag is then due to pressure drag, increasing as the front area normal to the flow increases. C_M of F45a confirms that the section is not behaving like an airfoil due to the extreme buffeting, as C_M is increasing almost linearly and does not have a plateau. The section then recovers airfoil-like behavior for the F45b case, resembling what was observed for the most turbulent homogeneous cases earlier to some degree.
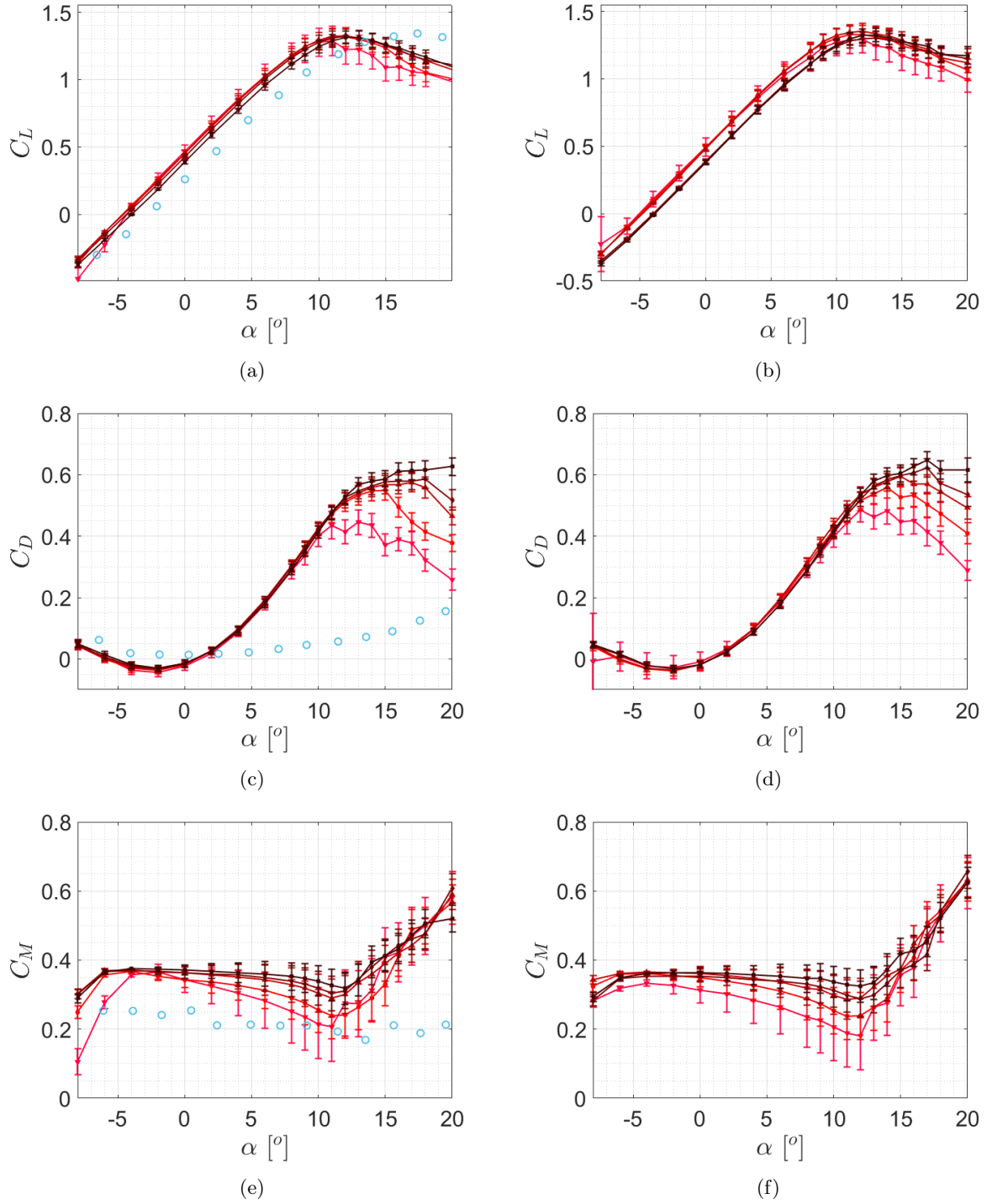
Figure 8: Lift (a), drag (c) and moment (e) coefficients at $T_i = 1.11\%$ and lift (b), drag (d) and moment (f) coefficients at $T_i = 1.99\%$ with increasing color intensity corresponding to increasing Re_c: $Re_c = 1.0 \times 10^5 (\square)$, $Re_c = 2.0 \times 10^5 (\bullet)$, $Re_c = 3.1 \times 10^5 (\triangle)$, $Re_c = 3.5 \times 10^5 (\diamond)$, $Re_c = 4.1 \times 10^5 (\triangledown)$. The errorbars represent the propagation of error from the instruments, and ($\circ$) are NACA4412 coefficients from Ostowari and Naik (1985) at $Re_c = 2.5 \times 10^5$.
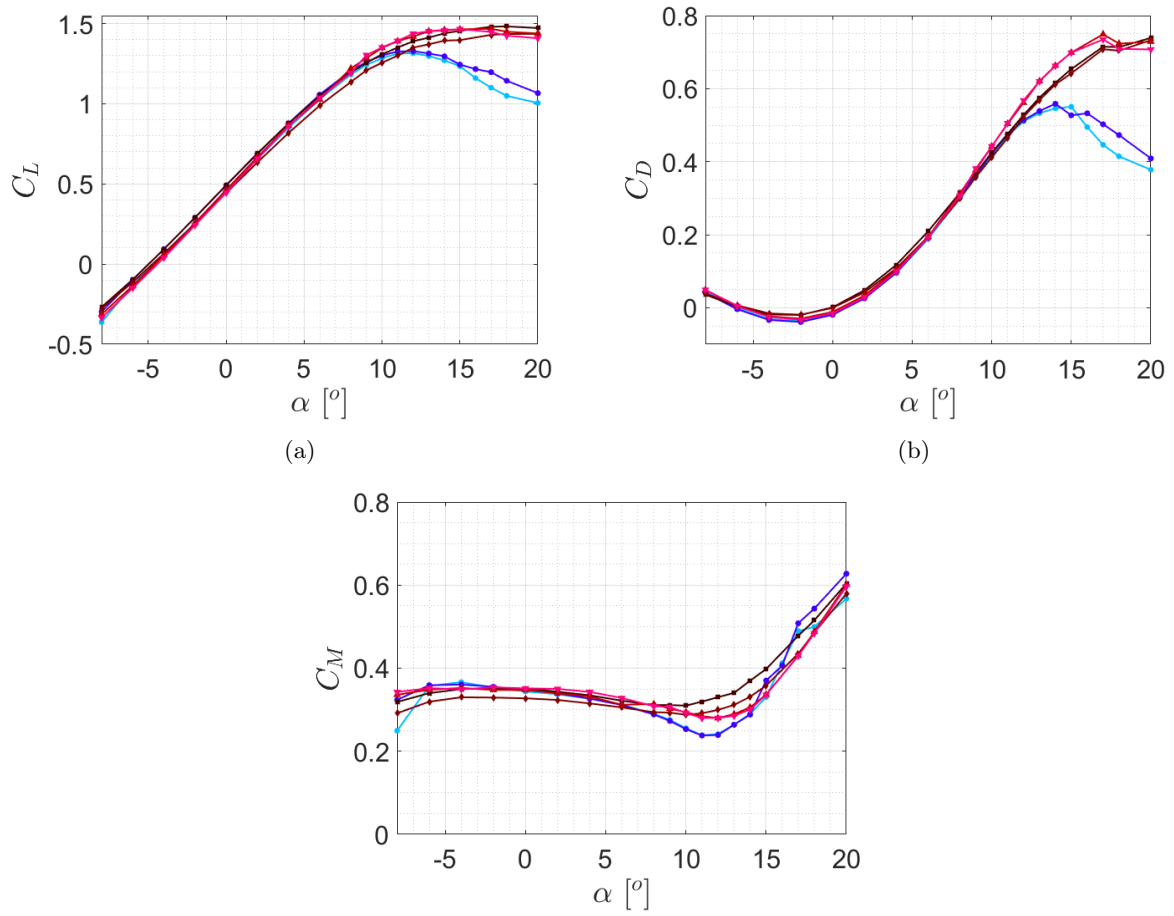
17

Figure 9: Lift (a), drag (b) and moment (c) coefficients of the airfoil subjected to homogeneous turbulence at $Re_c = 2.0 \times 10^5$ with increasing color intensity corresponding to increasing T_i: $T_i = 10.9\%(\triangledown)$, $T_i = 11.6\%(\triangle)$, $T_i = 16.4\%(\diamondsuit)$, $T_i = 17.5\%(\square)$ and $T_i = 1.11\%(\bullet)$, $T_i = 1.99\%(\bullet)$.
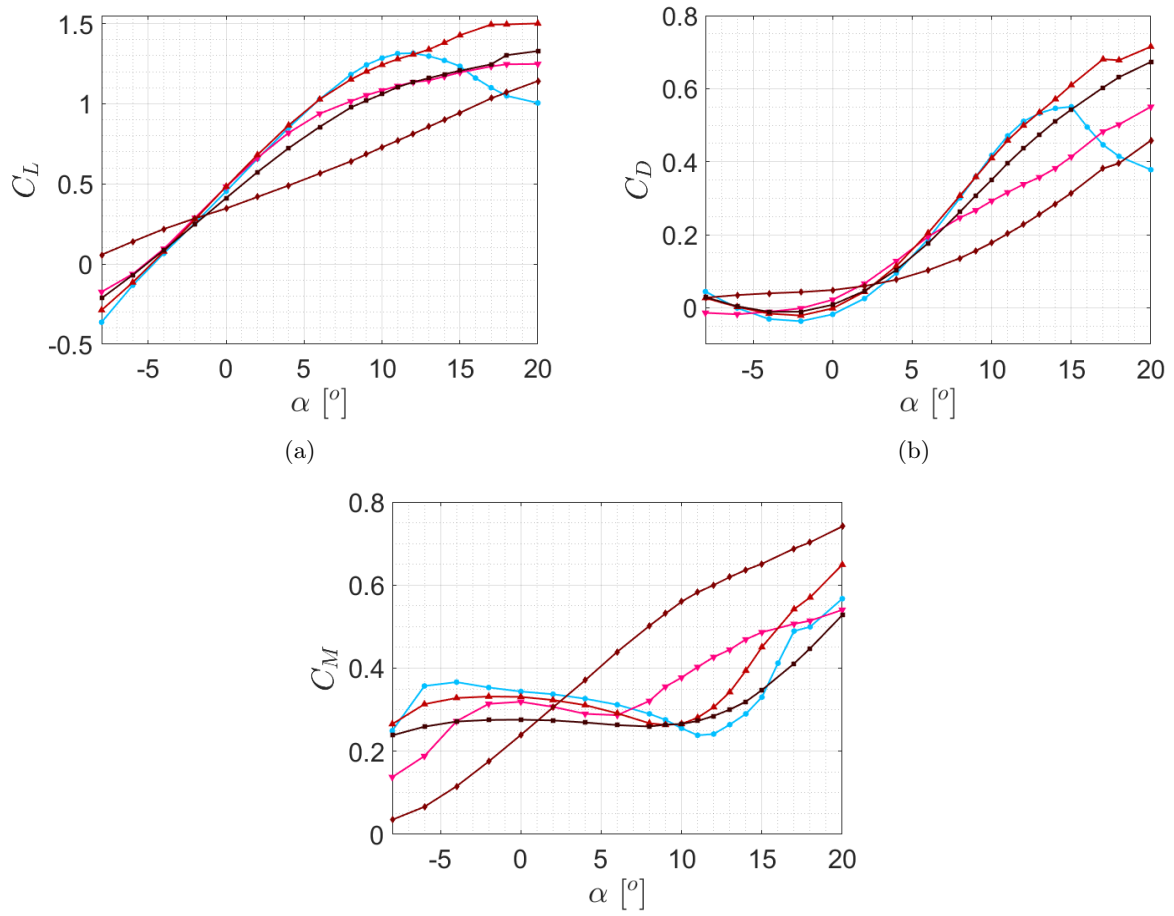
18

(a)

(b)

Figure 10: Lift (a), drag (b) and moment (c) coefficients of the airfoil subjected to periodic turbulence at $Re_c = 2.0 \times 10^5$ with increasing color intensity (light to dark) corresponding to increasing T_i of cases: F15a($\triangledown$), F15b($\triangle$), F45a($\diamond$), F45b($\square$) and REF($\bullet$).
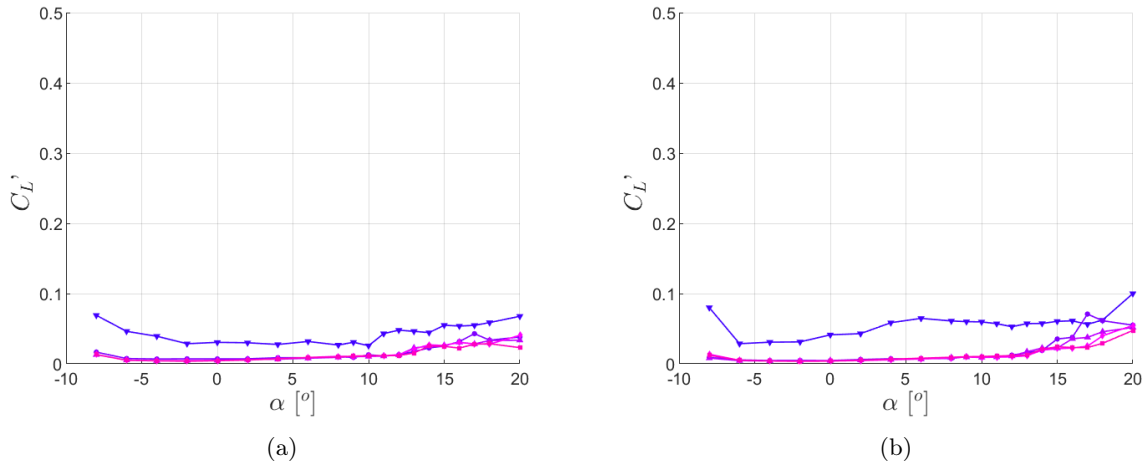
Figure 11: Standard Deviation of the time-series reported to C_L for (a) $T_i = 1.11\%$ and (b) $T_i = 1.99\%$ for all α with color intensity corresponding to increasing Re_c: $Re_c = 1.0 \times 10^5 (\triangledown)$, $Re_c = 2.0 \times 10^5 (\circ)$, $Re_c = 3.1 \times 10^5 (\triangle)$, $Re_c = 3.5 \times 10^5 (\diamond)$ and $Re_c = 4.1 \times 10^5 (\square)$.

6 Time-series analysis and vibrations

Due to observations of significant vibrations and buffeting of the airfoil, the standard deviation of the time-series and the Power Spectral Density are analysed in this section. This is done to gain insight on how the aeroelastic airfoil responds to the different incoming turbulent conditions, and how the energy is transmitted from the turbulence to the airfoil.

6.1 Time domain analysis

The standard deviation of the lift coefficient, C_L', from the time-series for the two Reynolds number scans cases at $T_i = 1.11\%$ and $T_i = 1.99\%$ are shown in Figure 11a and Figure 11b, respectively. C_L' relates directly to the energy content of the vibrations of the airfoil, and thus the damaging potential of the vibrations. For both cases, increasing Re_c tends to decrease C_L', suppressing almost all vibration in the linear C_L section (from section 5). This stiffening effect is in accordance with Goyaniuk et al (2020) and Poirel and Mendes (2014). Stall induced vibrations is also observable here, with C_L' increasing at high negative and positive α. It is unclear whereas the stall induced vibrations are actually stall flutter as the flow patterns around the airfoil were not investigated. Even if it is strongly suspected that the increase in vibration is due to stall flutter, it will only be referenced to as stall induced vibrations here. The Re_c dependence of stall discussed in subsection 5.1 is also observable here, with C_L' increasing at higher α for higher Re_c, indicating that flow separation is retarded as the Reynolds number increases. Increasing T_i from 1.11% to 1.99% also increased C_L', with generally higher C_L' for $Re_c = 1.0 \times 10^5$, and higher C_L' for the other cases at post stall α. however, the increase of T_i did not seem to have an impact on the pre-stall region of higher Re_c. It is suspected that T_i is low enough to enable a laminar boundary layer on a significant portion of the airfoil, as reported by Goyaniuk et al (2020). At post-stall, the boundary layer detaches and C_L' becomes higher for the higher T_i.

C_L' for the homogeneous, isotropic FST of Table 1 are presented in Figure 12a. C_L' is relatively constant for $\alpha \leq 10°$, and then increases drastically as α increases. This plateau at lower α indicates that the lift variation depends only on the turbulence properties, before stall induced vibrations starts to amplify C_L' as α increases. It can be noted that H18 does not follow the trend of the other cases, with lower C_L' than for H16, even if T_i and u'/w' are higher than for all other cases. The lower C_L' for H18 can be explained by the turbulence length scale, where $L_{ux}/c = 2$ (from Table 1). With length scales significantly larger than the chord length of the airfoil, the entrainment of the flow in the boundary layer is less efficient (Vita
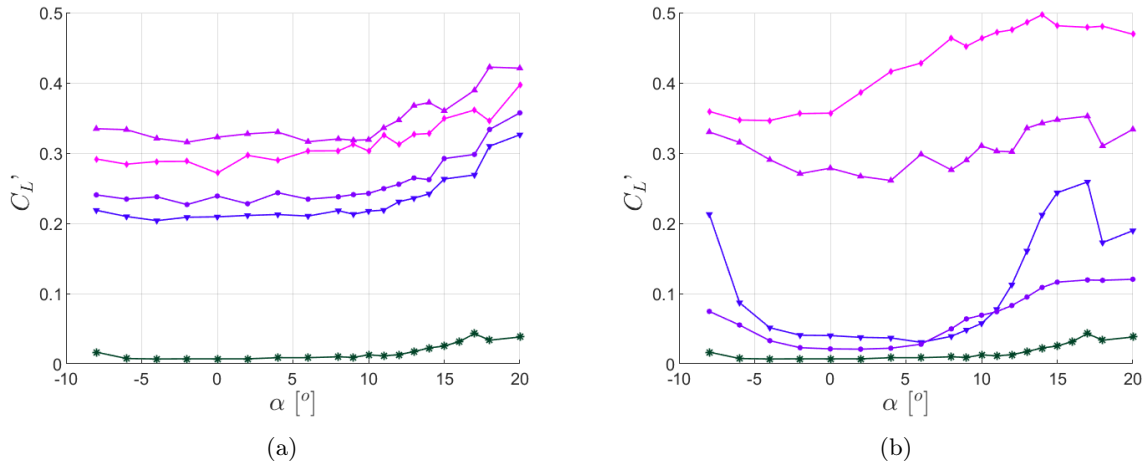
Figure 12: Standard Deviation of the time-series reported to C_L with color intensity corresponding to increasing T_i for (a) homogeneous FST and: H11($\triangledown$), H12($\circ$), H16($\triangle$), H18($\diamondsuit$) and (b) periodic FST and: F15a($\triangledown$), F15b($\circ$), F45a($\diamondsuit$), F45b($\triangle$) and REF(*).

et al, 2020). A direct relation between T_i and C'_L for the other homogeneous cases with a length scale $L_{ux} < 1.5c$ is observed. Figure 13 presents the mean C'_L of the linear region of the homogeneous cases as a function of T_i. C'_L increases linearly with a slope of $0.0225/T_i$ before the effect of large turbulence scale reduces the last point. This linear increase of C'_L was also noted by Li et al (2021), even though they did not investigate the effect of the length scales.

Figure 12b shows C'_L for the periodic FST cases. A clear difference can be seen between the two different flapping angles. F15a and F15b have very low and constant C'_L in their C_L linear region, with $C'_L = 0.037$ and $C'_L = 0.020$, respectively. This indicates that the flow stays attached on a consequent portion of the airfoil. Outside the linear region, C'_L is consequently increased. The lift coefficient deviations are much higher than for low intensity turbulent flow, thus the periodic turbulence is accentuating the stall induced vibrations. This is true for F15a, where low frequencies amplify even more the vibrations. It is unclear why $\alpha = 18°$ and $20°$ has a decrease in C'_L, but a detachment of the alternating vortices along the airfoil's surface amplifying stall flutter is suspected. For the $\theta = 45°$ cases, all C'_L have a high value. The boundary layer is suspected to be totally detached for these cases due to the strong buffeting. F45a has the highest $C'_L = 0.5$, which almost constantly increased as the front surface area increases, giving a larger surface for the eddies to encounter. The F45b case have a slightly decreasing trend for α of the linear region with $C'_L = 0.26$ at $\alpha = 4°$, with a behavior in between the $\theta = 15°$ cases and the homogeneous FST cases, supporting the argument towards a randomisation of the turbulence.

6.2 Frequency domain analysis

ϕ_L of REF is shown in Figure 14a. As was discussed in section 4, ϕ_L is computed from load cell 1, in order to show the frequencies above the resonance frequency f_r. The number of bins used to compute the PSD was reduced to 2^8 as the sampling time of REF was lower. Immediately, it can be noted that the main two peaks in ϕ_L are located at the same frequencies $f_r = 6.5$ Hz and $f_v = 24$ Hz as the shock-excitation test of section 4. The frequencies appear to be independent of the freestream velocity, thus they were not normalized. The 17 Hz $< f <$ 22 Hz region is also less clear with a generally high agitation, and what appears to be three additional small peaks at $f_2 = 16.4$ Hz, $f_3 = 18.7$ Hz and $f_4 = 21$ Hz. For $\alpha > \alpha_{crit}$, ϕ_L is increased substantially for all frequencies under f_2, with ϕ_L ranging from $\phi_L = 1 \times 10^{-2}$ around $\alpha = 0°$ to $\phi_L = 2 \times 10^{-1}$ for $\alpha = 20°$ at f_r. This increase in ϕ_L is a consequence of the stall induced vibrations starting to appear with partial or complete breakaway of the flow from the airfoil periodically during the oscillation as reported by Dimitriadis and Li (2009). It is important to note
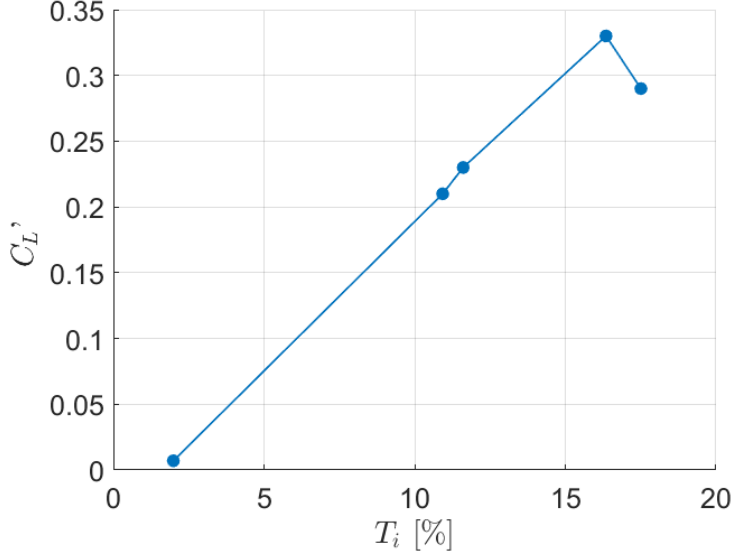
Figure 13: Lift deviation dependence on the turbulence intensity of homogeneous FST cases in the linear region.

that the essential feature of stall flutter is the nonlinear aerodynamic reaction to the vibrating airfoil section, with a mechanism for energy transfer from the flow to the airfoil not relying on elastic and/or aerodynamic coupling between two modes. Above f_2, ϕ_L is still higher with increasing α, but the curves are closer to each other, with a ϕ_L variation of the order 10^1. It is unclear where f_v, f_2, f_3 and f_4 have their source from as they appeared for lower vibration amplitudes in section 4. It is possible that these peaks come from a response of the forced vibration rig, which was observed to vibrate outside of the wind tunnel, especially when the flow was highly turbulent. Their presence though, can't be ignored, as they have an effect of increasing the collapse of ϕ_L for different α.

ϕ_L of H2 is shown in Figure 14b. f_r and f_v remain unchanged. For $\alpha < \alpha_{crit}$, ϕ_L behaves similarly to REF. This is in accordance with what was described in subsection 6.1, where no difference was noted in C_L' pre-stall. For $\alpha > \alpha_{crit}$ the change in ϕ_L is significant and more marked than for REF, with a PSD ranging from $\phi_L = 1 \times 10^{-2}$ around $\alpha = 0°$ to $\phi_L = 1 \times 10^0$ for $\alpha = 20°$ at f_r. This is also a sign that the stall induced vibrations becomes more violent for H2, as more energy is transmitted from the FST to the airfoil. f_2 is no longer observable, but f_3 and f_4 remain unchanged, with peaks more distinct than for REF.

ϕ_L for the H18 case is shown in Figure 15a. For higher FST cases, the bins were increased back to 2^{11}. This was allowed by a higher sampling time, also allowing to show the smallest frequencies. For all α, ϕ_L curves are much higher than for REF indicating higher vibrations. A clear change is the existence of a plateau from $f = 0.5$ Hz to $f = 1.5$ Hz. Before this plateau, a clear distinction of higher ϕ_L for higher α can be seen, with a change of an order of magnitude between $\alpha = 0°$ and $\alpha = 20°$. All ϕ_L increases to around 1×10^1 at the plateau, then ϕ_L for all α returns to a value similar to what it was before the plateau for the highest α. Interestingly, the starting frequency of the plateau is equal to the shafts rotating frequency, $\Omega = 0.5$ Hz (Table 1). This indicates that even if the FST is homogeneous and isotropic, a trace from the ATG influence is still present in the turbulence. ϕ_L is similar for all α at higher f, indicating that the increase in C_L' at high α is caused by the change in low frequency excitation before the plateau. f_r and f_v are unchanged here, with $\phi_{L,r} = 2 \times 10^1$ and $\phi_{L,v} = 3 \times 10^{-1}$. The other three frequencies are slightly decreased to $f_2 = 16.2$ Hz, $f_3 = 17.2$ Hz and $f_3 = 20.9$ Hz and their respective amplitude compared to $\phi_{L,v}$ unchanged from REF. The plateau starting at $f = \Omega$ can also be seen for H16 in Figure 15b. The same behavior of ϕ_L is observed, with lower PSD for low α
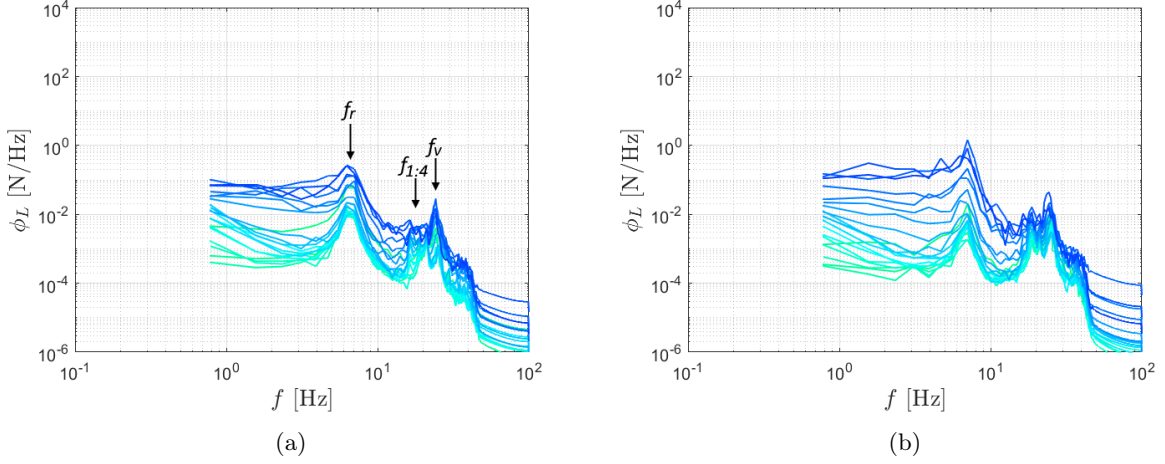
Figure 14: Lift power spectral density of REF (a) and H2 (b) from load cell 1 for all α.

before the plateau, and a convergence of the curves to a similar level, both at and after the plateau. It is slightly harder to see that the PSD return to a ϕ_L similar than for the highest α after the plateau, but a decrease is clearly observable. f_r, f_v, f_2, f_3 and f_4 all remain unchanged from H18. The C'_L of H16 is lower than for H18, since its plateau is located at higher frequencies, which are less energetic.

In Figure 16a for H12, $\Omega = 5$ Hz is close to $f_r = 6.5$ Hz. This proximity to the resonance frequency results in no plateau observable for ϕ_L. Interestingly, this did not result in a higher $\phi_{L,r}$ (the corresponding lift power spectral density at the give point) nor C'_L, even if an excitation of a structure with a frequency close to the resonance frequency (or any harmonics) should result in a powerful amplification of the vibrations. This might be because turbulence is broadband, and even if it has a dominant frequency, there are still many other frequencies with significant content that it washes out the effects. The region below f_r is relatively scattered, as no plateau or peak is present to collapse the curves together. The absence of a plateau here does not seem to influence the behavior of C'_L, as was the case for homogeneous FST. $\phi_{L,r} = 2 \times 10^1$ and $\phi_{L,v} = 3 \times 10^{-1}$ is similar than for H16 and H18. As the frequencies passes f_r, the curves are regrouped together. having Ω close to f_r has an impact on the frequency peaks $f_2 = 14$ Hz, $f_3 = 16.6$ Hz and $f_4 = 20.8$ Hz with $\phi_{L,2} = 2 \times 10^{-1}$, $\phi_{L,3} = 1 \times 10^{-1}$ and $\phi_{L,4} = 5 \times 10^{-1}$, which is higher than f_v. The change in these frequencies when Ω is higher than f_r is confirmed by Figure 16b, where $f_2 = 13.8$ Hz, $f_3 = 16.4$ Hz, $f_4 = 19.1$ Hz and the apparition of $f_5 = 20.8$ Hz with $\phi_{L,2}$ unchanged, $\phi_{L,3} = 1 \times 10^0 = \phi_{L,4} = \phi_{L,5}$, while f_r, f_v and their respective densities remains unchanged.

In general, the FST created by the grid increased ϕ_L to equal levels for all the homogeneous ATG cases. The resonance frequency f_r, the second peak observed at small oscillations f_v and their corresponding densities remained unchanged across the cases. Depending on the oscillation frequencies of the shafts Ω, a plateau appeared starting at $f = \Omega$ for frequencies inferior to the resonance frequency, while for $\Omega > f_r$, the small peaks before f_v were affected. As the excited region goes towards lower frequencies, the buffeting amplitude is increased.

6.3 Periodic cases

As the ATG is operating periodically, some of the frequencies are significantly excited than for the homogeneous cases. Once again, a relation between ϕ_L and the frequency of the ATG f_f can be noted. For F15a presented in Figure 17a, the first peak frequency is $f_p = f_f = 0.4$ Hz. This first peak is then followed by other peaks which are positive integer multiple of the frequency of the original frequency, i.e. harmonics. The curves also have a general increase around $f_r = 6.5$ Hz and $f_v = 24$ Hz, indicating that the resonance frequency and the higher frequency have not been totally suppressed. This suggests that the airfoil subjected to periodic flows has two distinct responses. One directly connected to the
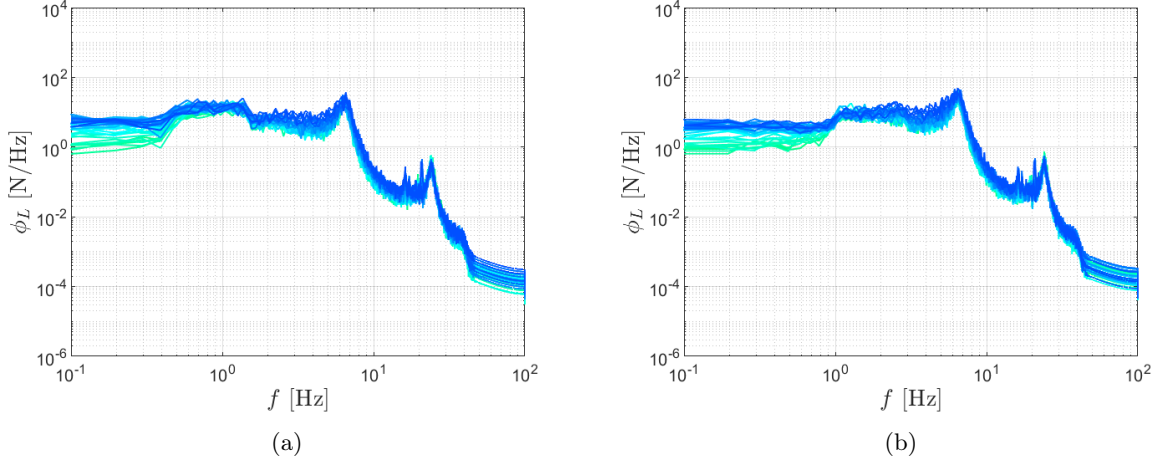
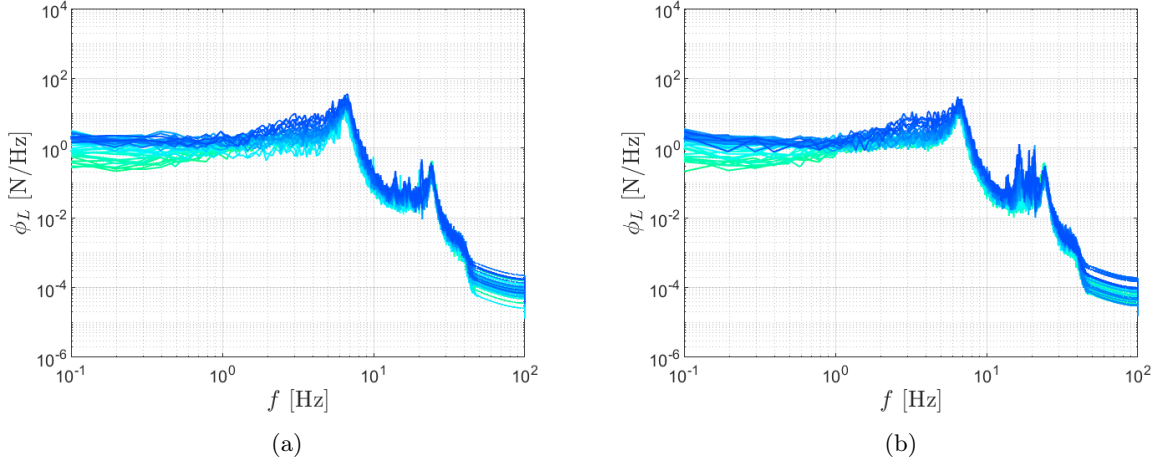Figure 15: Lift power spectral density of H18 (a) and H16 (b) from load cell 1 for all α.

Figure 16: Lift power spectral density of H12 (a) and H11 (b) from load cell 1 for all α.

FST and its properties, and one as a result of natural response of the airfoil. Since the turbulence is not random, specific frequencies are significantly more excited, giving $\phi_{L,p} = 3 \times 10^2$. An important note is that the harmonics are present for all α at frequencies that are an even integer multiple of f_p. For odd integer multiples, only α outside of the linear region of C_L present a peak. This is observable for the first peaks, but this effect is present for all the harmonics, except regions around f_r and f_v where the natural response dominates. This even-odd relation between α and the harmonics is also present for case F15b in Figure 17b. here, $f_p = 3.6$ Hz is slightly lower than $f_f = 4$ Hz, but corresponds to the oscillating frequency of the flow velocity recorded by the hot-wire probe. The slight increase around f_r, followed by a decrease and a peak around f_v can also be observed here, but the first harmonic at $f_{h1} = 7.1$ Hz with $\phi_{L,h1} = 2 \times 10^2$ suppresses f_r almost totally. Before f_p, there is a distinct separation of the spectrum of post-stall α from other α, similar to the REF case. This is due to few perturbations with a frequency lower than what the ATG produced, and indicates that the flow is actually strongly periodic for both F15 cases.

With a flapping angle of 45°, the flow is more blocked through the ATG and stronger, less regular gusts are present. Figure 18a shows the PSD of F45a. The same general trends as for F15a can be observed, with a fundamental frequency $f_p = 3.6$ Hz and $\phi_{L,p} = 12 \times 10^2$, and harmonics with an even-odd
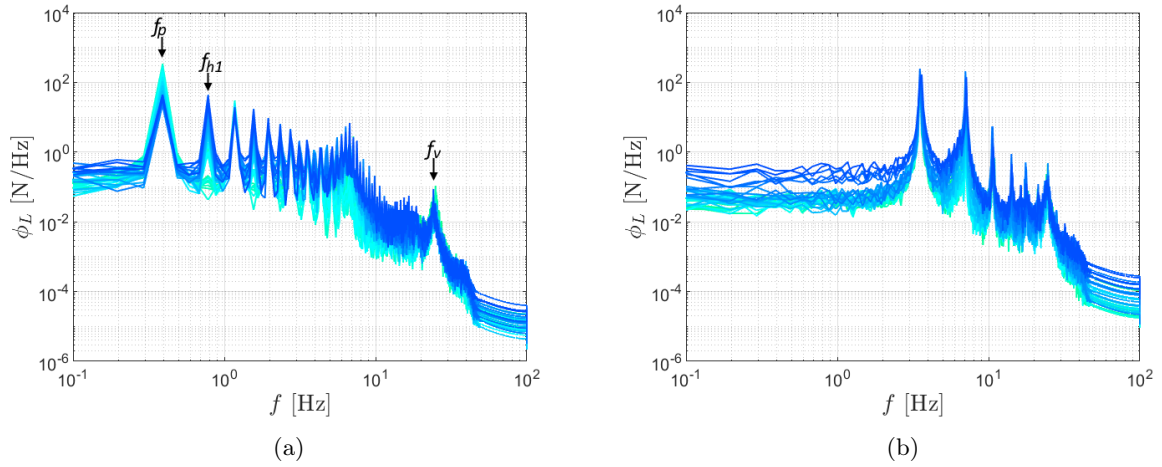
24

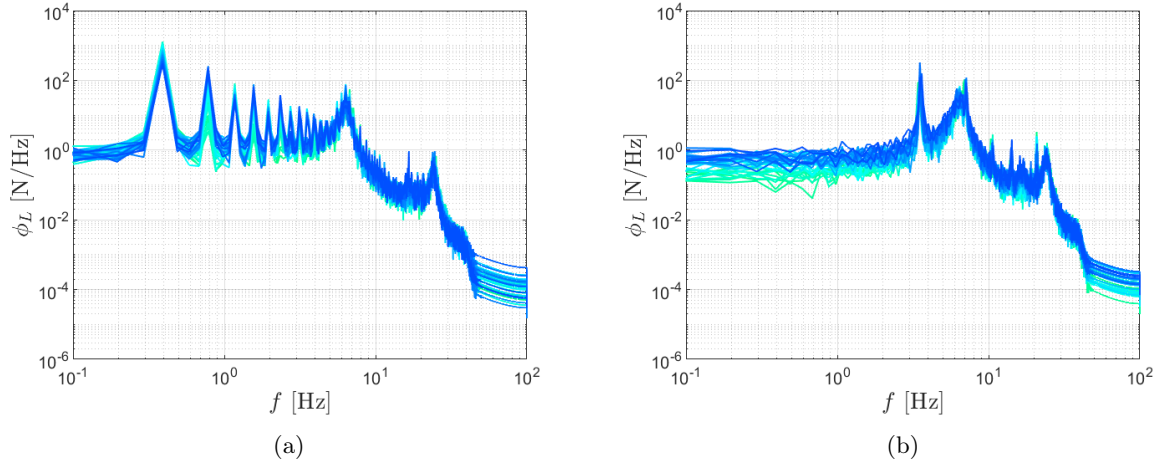Figure 17: Lift power spectral density of F15a (a) and F15b (b) from load cell 1 for all α.

Figure 18: Lift power spectral density of F45a (a) and F45b (b) from load cell 1 for all α.

integer multiple dependency on α of the C_L linear region. However, the spectrum for low α present here harmonics for all integer multiples of f_p, but their spectrum still remains lower for even ones. With 45° flapping cases, the amplitude of the harmonic's PSD is reduced towards higher frequencies, with the curves behavior resembling what the random operation of the ATG produced. This could mean that the higher frequency FST tends to collapse, randomising to a certain extent the behavior of the flow. Supporting this theory is the apparition of a peak $f_3 = 16.6$ Hz at the same location as the homogeneous cases. This collapse of the periodicity can also be seen in Figure 18b for F45b. Here, only the fundamental frequency, $f_p = 3.6$ Hz stands out with $\phi_{L,p} = 3 \times 10^2$. The four harmonics are still present, but are not dominant here as was the case for F15b. Indeed, the first harmonic at $f_{h1} = 7$ Hz, is almost covered by the resonance frequency of the airfoil $f_r = 6.5$ Hz. There is also a resurgence of a gentle peak at $f_2 = 16.4$ Hz, $f_3 = 19$ Hz and $f_4 = 20.9$, corresponding to the higher frequency peaks of the homogeneous cases.

25

7   Further work and possible improvements

For α close to 0°, the C_D curves in Figure 8c to Figure 10b are slightly negative. This is due to a small mismatch error of the α between the mass scans and the test cases. This was not presented in the errorbars, which only represent the propagation of error from the instruments. A mismatch of $\alpha\pm0.5°$ would give a change $\Delta C_D = \pm0.032$, enough to bring the C_D curve above zero. Similarly, $\Delta C_L = \pm0.018$ and $\Delta C_M = \pm0.004$ at $U_\infty = 5$m/s which are still acceptable values compared to the range of the coefficients. Nonetheless, to avoid this error, the mass scan should be done every time the model is taken on and off, and not only once as we did here.

Another source of error is the deformation of the skin at high α with either high flow velocity or high FST. The skin solution with an iron-on polyester fabric was chosen due to the weight limitation of 7 kg for the range of the load cells. The airfoil weighted 4 kg in total, leaving some room for a stiffer skin. However, a more robust solution would have either increased the weight considerably, or been too complicated to implement by ourselves. A harder skin would also mean less vibration observable as the elasticity of the whole airfoil would have been reduced. This would have been interesting to look only into the aerodynamic properties, but the investigation of the vibrations gave a more realistic set-up of how airfoils actually operate and behave in strong turbulence.

The flapping cases of the ATG gave properties that were beyond those reliably measured with hot-wire anemometry. Those cases would be best to simulate periodic and gusty flow, with a limit of the flapping angle and/or of the flapping frequency f_f.

The load cells were in agreement with respect to the time-series of the vibrations and the lift spectra. Instead of using two load cells, one could use a combination of one accelerometer and one load cell, this would allow for insight into the displacements and dig more into the buffeting physics. In addition, the use of high speed imaging would allow the construction of a single-degree of freedom (SDOF) buffet model.

8 Conclusions

An aeroelastic airfoil was subjected to five homogeneous isotropic, and four periodic, active grid generated turbulent flows with varying turbulence properties. The airfoil was Reynolds number independent in the pre-stall region with $Re_c = 2.0 \times 10^5$.

The homogeneous turbulence characteristics were found to be representative of the FST, with T_i varying from the reference case at 1.11% and up to 17.5%. An increase in T_i caused a general increase in the maximum lift coefficient. The lift slope varied marginally, and increased for increasing T_i up to 12%, but became lower than for the reference case for the two most turbulent cases. The biggest impact was the increase of the maximum lift and the critical angle of attack for increasing T_i, ranging from $C_{L,max} = 1.32$ and $\alpha_{crit} = 12°$ at $T_i = 1.11\%$ to $C_{L,max} = 1.48$ and $\alpha_{crit} = 18°$ at $T_i = 17.5\%$. The standard deviation of the time-series was used to compute the lift coefficient fluctuations. For $T_i = 1.11\%$ and $T_i = 1.99\%$, the model only experienced stall induced vibrations, indicating that the turbulence was low enough to allow for an attached boundary layer on a significant portion of the airfoil at low α with a stiffening effect. For higher T_i, buffeting of the airfoil was recorded at all α. In the linear lift region, the lift fluctuations C'_L were found to have a linear increase for increasing T_i for turbulence length scale $L_{ux}/c < 1.5$, before stall induced vibrations occurred at higher angles of incidence. From the lift spectra, it was found that the resonance frequency f_r of the airfoil was independent both of the flow velocity and of the turbulence. However, turbulence brought the spectra of the different α closer together, and a relation between the PSD and the ATG was clearly observable. Frequencies around the shafts' rotating frequency Ω were amplified with a plateau appearing for $\Omega < f_r$.

For the periodic FST cases, the turbulence measurements are less reliable, due to suspiciously high T_i and less homogeneous flow. The flow is regarded as fluctuating with wind gusts, with higher fluctuations as the flapping frequency f_f of the ATG increases, and higher gusts amplitude with increasing flapping angle θ. The performance of the airfoil was strongly reduced with periodic FST. Lower f_f and higher θ degraded the performance even more. In contrast with homogeneous FST, no linear dependence of C'_L on T_i was found, even for the lowest periodicity where T_i was still reliably measured by the hot-wire. C'_L depended on the gusts frequency and intensity, and stall induced vibrations were amplified for the $\theta = 15°$ cases. This amplification of vibrations is due to the presence of harmonics in the PSD of the periodic cases, with a fundamental frequency $f_p = f_f$. All harmonics are present for high α, but only even integer multiples of f_p harmonics were present for low α. This distinction between high and low α is suspected to be caused by vortex shedding, amplified by the periodic FST.

Even if important sources of uncertainty are present in this work, the observed effects and the trends in behavior are still very informative. In the investigation of the dependence of the lift and drag, the lift variation and vibrations on the incoming flow, the novelty of this study provides insight on the effect of active grid-generated turbulence on an aeroelastic NACA4412 airfoil.

References

Bartl J, Sagmo KF, Bracchi T, Sætran L (2019) Performance of the NREL S826 airfoil at low to moderate Reynolds numbers—A reference experiment for CFD models. European Journal of Mechanics - B/Fluids 75:180–192, DOI https://doi.org/10.1016/j.euromechflu.2018.10.002

Brahma P, Mukherjee S (2010) A realistic way to obtain equivalent Young's modulus of layered soil. Indian Geotechnical Conference GEOtredz pp 305–308

Bruun HH (1995) Hot-wire Anemometry. Oxford University Press

Cao N, Ting DSK, Carriveau R (2011) The performance of a high-lift airfoil in turbulent wind. Wind Engineering 35(2):179–196, DOI 10.1260/0309-524X.35.2.179

Cekli HE, van de Water W (2010) Tailoring turbulence with an active grid. Experiments in Fluids 49(2):409–416, DOI 10.1007/s00348-009-0812-5

Cigada A, Falco M, Zasso A (2001) Development of new systems to measure the aerodynamic forces on section models in wind tunnel testing. Journal of Wind Engineering and Industrial Aerodynamics 89(7):725–746, DOI https://doi.org/10.1016/S0167-6105(01)00075-7, 10th International Conference on Wind Engineering

Comte-Bellot G, Corrsin S (1966) The use of a contraction to improve the isotropy of grid-generated turbulence. Journal of Fluid Mechanics 25(4):657–682, DOI 10.1017/S0022112066000338

Dessi D, Mastroddi F (2008) A nonlinear analysis of stability and gust response of aeroelastic systems. Journal of Fluids and Structures 24(3):436–445, DOI https://doi.org/10.1016/j.jfluidstructs.2007.09.003

Devinant P, Laverne T, Hureau J (2002) Experimental study of wind-turbine airfoil aerodynamics in high turbulence. Journal of Wind Engineering and Industrial Aerodynamics 90(6):689 – 707, DOI https://doi.org/10.1016/S0167-6105(02)00162-9

Dimitriadis G, Li J (2009) Bifurcation behavior of airfoil undergoing stall flutter oscillations in low-speed wind tunnel. AIAA Journal 47(11):2577–2596, DOI 10.2514/1.39571

Divincenzo N (2020) Natural frequency and resonance. URL http://web.archive.org/web/20080207010024/http://www.808multimedia.com/winnt/kernel.htm

dos Santos L, Marques F (2021) Nonlinear aeroelastic analysis of airfoil section under stall flutter oscillations and gust loads. Journal of Fluids and Structures 102:103,250, DOI https://doi.org/10.1016/j.jfluidstructs.2021.103250

Fearnow DO (1951) Investigation of the structural damping of a full-scale airplane wing. official memorandum, National Advisory Committee for Aeronautics Collection, Washington, DC, USA, URL https://digital.library.unt.edu/ark:/67531/metadc58765/

Genç MS, Koca K, Açikel HH, Özkan, Gökhan, Kiris, Mehmet Sadik, Yildiz, Rahime (2016) Flow characteristics over NACA4412 airfoil at low Reynolds number. EPJ Web of Conferences 114:02,029, DOI 10.1051/epjconf/201611402029, URL https://doi.org/10.1051/epjconf/201611402029

Goyaniuk L, Poirel D, Benaissa A (2020) Pitch–heave symmetric stall flutter of a NACA0012 at transitional Reynolds numbers. AIAA Journal 58(8):3286–3298, DOI 10.2514/1.J059008

Han Y, Liu S, Hu J, Cai C, Zhang J, Chen Z (2014) Experimental study on aerodynamic derivatives of a bridge cross-section under different traffic flows. Journal of Wind Engineering and Industrial Aerodynamics 133:250–262, DOI https://doi.org/10.1016/j.jweia.2014.08.003

Hearst RJ (2019) The use of active grids in experimental facilities. In: Örlü R, Talamelli A, Peinke J, Oberlack M (eds) Progress in Turbulence VIII, Springer International Publishing, Cham, pp 173–178, URL https://link.springer.com/chapter/10.1007/978-3-030-22196-6_27

Hearst RJ, Lavoie P (2015) The effect of active grid initial conditions on high Reynolds number turbulence. Experiments in Fluids 56(10):185, DOI 10.1007/s00348-015-2052-1

Hodges DH, Pierce GA (2011) Introduction to Structural Dynamics and Aeroelasticity, 2nd edn. Cambridge Aerospace Series, Cambridge University Press, DOI 10.1017/CBO9780511997112

Huang RF, Lee HW (1999) Effects of freestream turbulence on wing-surface flow and aerodynamic performance. Journal of Aircraft 36(6):965–972, DOI 10.2514/2.2537

Istvan MS, Kurelek JW, Yarusevych S (2018) Turbulence intensity effects on laminar separation bubbles formed over an airfoil. AIAA Journal 56(4):1335–1347, DOI 10.2514/1.J056453

Koca K, Genç MS, Açıkel HH, Çağdaş M, Bodur TM (2018) Identification of flow phenomena over naca 4412 wind turbine airfoil at low reynolds numbers and role of laminar separation bubble on flow evolution. Energy 144:750–764, DOI https://doi.org/10.1016/j.energy.2017.12.045

Larssen JV, Devenport WJ (2011) On the generation of large-scale homogeneous turbulence. Experiments in Fluids 50(5):1207–1223, DOI 10.1007/s00348-010-0974-1, URL https://doi.org/10.1007/s00348-010-0974-1

Li L, Hearst RJ (2021) The influence of freestream turbulence on the temporal pressure distribution and lift of an airfoil. Journal of Wind Engineering and Industrial Aerodynamics 209:104,456, DOI https://doi.org/10.1016/j.jweia.2020.104456

Li M, Li M, Sun Y (2021) Effects of turbulence integral scale on the buffeting response of a long-span suspension bridge. Journal of Sound and Vibration 490:115,721, DOI https://doi.org/10.1016/j.jsv.2020.115721, URL https://www.sciencedirect.com/science/article/pii/S0022460X20305514

Maldonado V, Castillo L, Thormann A, Meneveau C (2015) The role of free stream turbulence with large integral scale on the aerodynamic performance of an experimental low Reynolds number S809 wind turbine blade. Journal of Wind Engineering and Industrial Aerodynamics 142:246 – 257, DOI https://doi.org/10.1016/j.jweia.2015.03.010

Mücke T, Kleinhans D, Peinke J (2011) Atmospheric turbulence and its influence on the alternating loads on wind turbines. Wind Energy 14(2):301–316, DOI https://doi.org/10.1002/we.422

Ostowari C, Naik D (1985) Post-stall wind tunnel data for NACA 44XX series airfoil sections. Tech. rep., Texas A and M Univ., College Station (USA). Dept. of Aerospace Engineering, DOI 10.2172/5791328

Poirel D, Mendes F (2014) Experimental small-amplitude self-sustained pitch–heave oscillations at transitional Reynolds numbers. AIAA Journal 52(8):1581–1590, DOI 10.2514/1.J052541, URL https://doi.org/10.2514/1.J052541

Pope SB (2000) Turbulent Flows. Cambridge University Press, DOI 10.1017/CBO9780511840531

Qiu Z, Wang F (2020) Aeroelastic responses of airfoil under dynamic stall forced to oscillate by cyclic pitch input. Journal of Sound and Vibration 479:115,366, DOI https://doi.org/10.1016/j.jsv.2020.115366

Qu Q, Jia X, Wang W, Liu P, Agarwal RK (2014) Numerical study of the aerodynamics of a naca 4412 airfoil in dynamic ground effect. Aerospace Science and Technology 38:56–63, DOI https://doi.org/10.1016/j.ast.2014.07.016

Ravi S, Watkins S, Watmuff J, Massey K, Peterson P, Marino M (2012) Influence of large-scale freestream turbulence on the performance of a thin airfoil. AIAA Journal 50(11):2448–2459, DOI 10.2514/1.J051640

Sarlak H, Mikkelsen R, Sarmast S, Sørensen JN (2014) Aerodynamic behaviour of NREL S826 airfoil at Re=100,000. Journal of Physics: Conference Series 524:012,027, DOI 10.1088/1742-6596/524/1/012027

Shannon C (1949) Communication in the presence of noise. Proceedings of the IRE 37(1):10–21, DOI 10.1109/JRPROC.1949.232969

Siedziako B, Øiseth O, Rønnquist A (2017) An enhanced forced vibration rig for wind tunnel testing of bridge deck section models in arbitrary motion. Journal of Wind Engineering and Industrial Aerodynamics 164:152–163, DOI https://doi.org/10.1016/j.jweia.2017.02.011

Stack J (1931) Test in the variable density wind tunnel to investigate the effects of scale and turbulence on airfoil characteristics. Tech. rep., URL https://digital.library.unt.edu/ark:/67531/metadc54044/

Stewart RW (1979) The atmospheric boundary layer. World Meteorological Organization, Geneva, URL https://nla.gov.au/nla.cat-vn1380974

Swalwell K, Sheridan J, Melbourne W (2001) The effect of turbulence intensity on stall of the NACA 0021 aerofoil. 14th Australasian Fluid Mechanics Conference pp 941–944

Szepessy S, Bearman PW (1992) Aspect ratio and end plate effects on vortex shedding from a circular cylinder. Journal of Fluid Mechanics 234:191–217, DOI 10.1017/S0022112092000752

Vita G, Hemida H, Andrianne T, Baniotopoulos C (2020) The effect of the integral length scale of turbulence on a wind turbine aerofoil. Journal of Wind Engineering and Industrial Aerodynamics 204:104,235, DOI https://doi.org/10.1016/j.jweia.2020.104235

Vos R, Farokhi S (2015) Introduction to transonic aerodynamics, vol Fluid mechanics and its applications. Springer, DOI 10.1007/978-94-017-9747-4

Wang S, Zhou Y, Alam MM, Yang H (2014) Turbulent intensity and reynolds number effects on an airfoil at low reynolds numbers. Physics of Fluids 26(11):115,107, DOI 10.1063/1.4901969

West GS, Apelt CJ (1982) The effects of tunnel blockage and aspect ratio on the mean flow past a circular cylinder with reynolds numbers between 104 and 105. Journal of Fluid Mechanics 114:361–377, DOI 10.1017/S0022112082000202

Wu B, Chen X, Wang Q, Liao H, Dong J (2020) Characterization of vibration amplitude of nonlinear bridge flutter from section model test to full bridge estimation. Journal of Wind Engineering and Industrial Aerodynamics 197:104,048, DOI https://doi.org/10.1016/j.jweia.2019.104048

Young WC, Budynas RG (2002) Roark's Formulas for Stress and Strain. McGraw-Hill

Yuan W, Laima S, Chen WL, Li H (2021) External excitation effects on the flutter characteristics of a 2-dof rigid rectangular panel. Journal of Wind Engineering and Industrial Aerodynamics 209:104,486, DOI https://doi.org/10.1016/j.jweia.2020.104486

Zhou T, Dowell E, shan Feng S (2019) Computational investigation of wind tunnel wall effects on buffeting flow and lock-in for an airfoil at high angle of attack. Aerospace Science and Technology 95:105,492, DOI https://doi.org/10.1016/j.ast.2019.105492
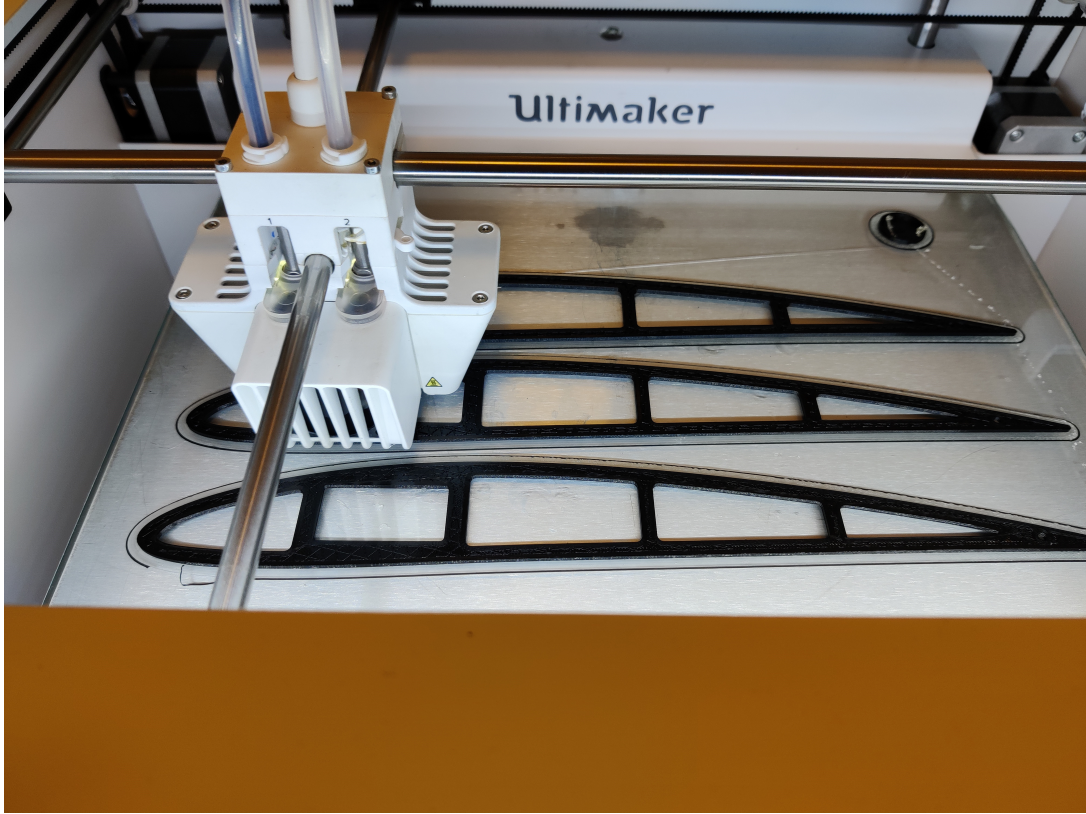
Appendix

A   Airfoil construction

Figure 19: 3D printing of the NACA4412 ribs

Figure 20: NACA4412 ribs with mounts to the spar

Figure 21: Mounting of the ribs to the spar

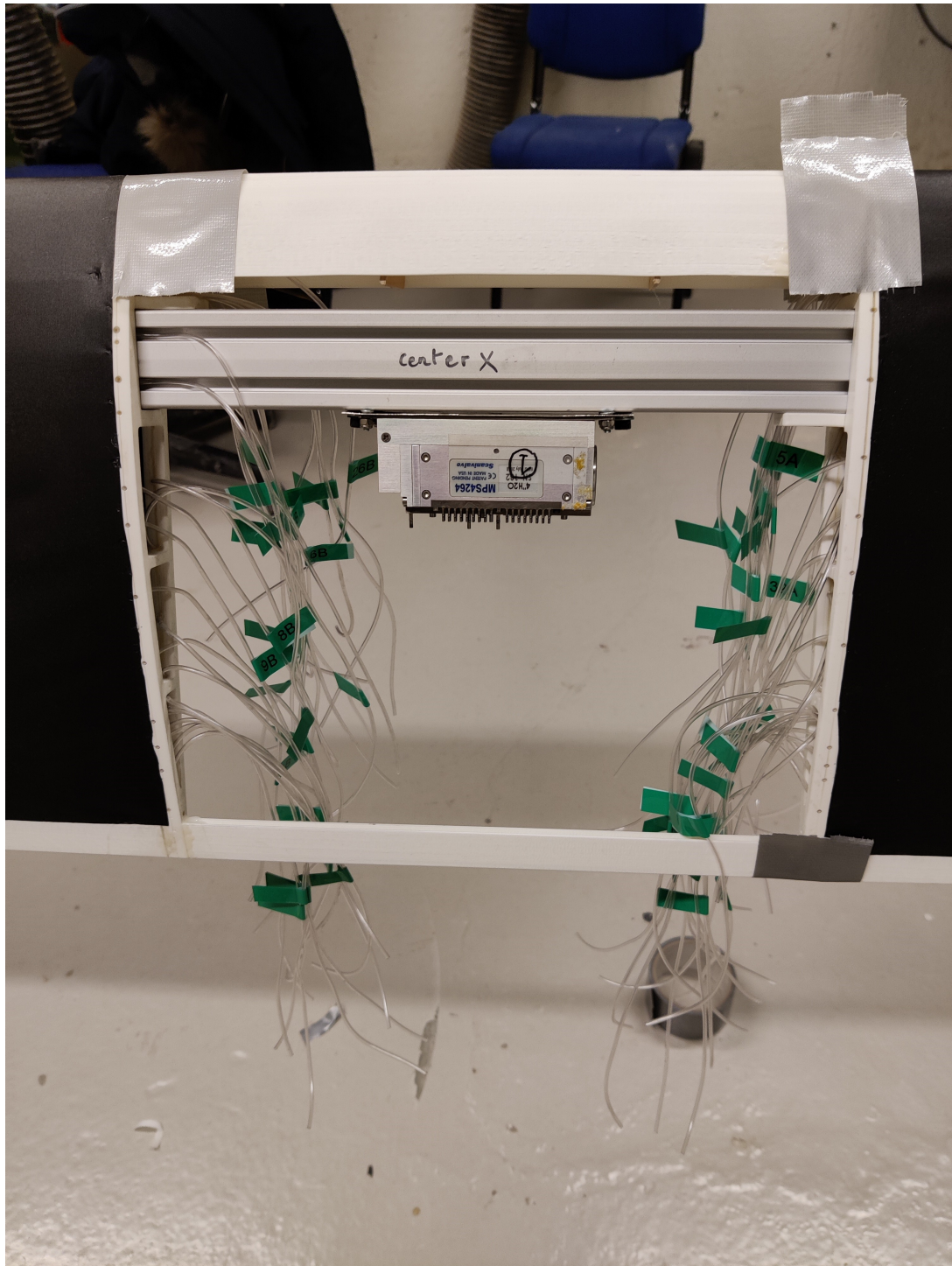Figure 22: Mounting of the leading edge and trailing edge structure

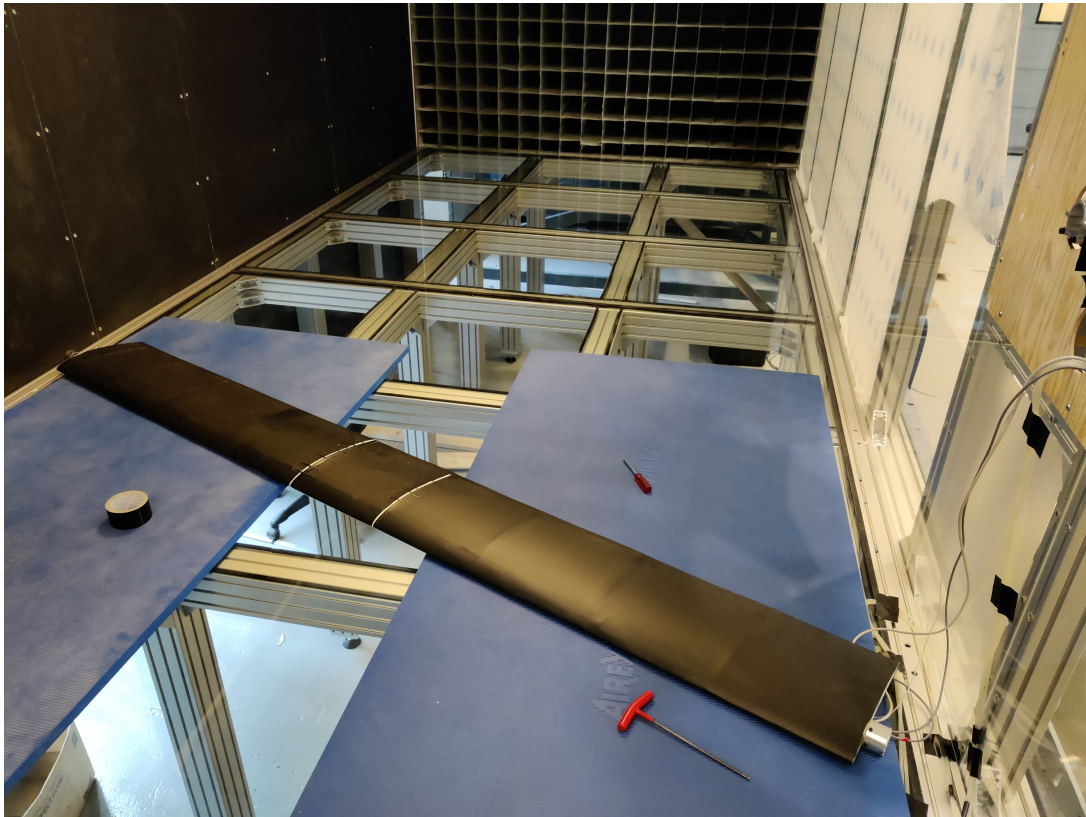Figure 23: Pressure transducer in the centre of the airfoil for another experiment

Figure 24: Airfoil section ready to be mounted on the forced vibration rig